Ribonucleoprotein condensation driven by retrotransposon LINE-1 sustains RNA integrity and translation in mouse spermatocytes

Chiara De Luca[1], Anuj Gupta[2] and Alex Bortvin[1,3,*]

[1] Carnegie Institution for Science, Department of Embryology, Baltimore, MD, USA

[2] The Sidney Kimmel Comprehensive Cancer Center, Baltimore, MD, USA

[3] Lead Contact

*Correspondence: bortvin@carnegiescience.edu

Summary

Transposable elements (TE) are mobile DNA sequences whose excessive proliferation endangers the host. Although animals have evolved robust TE-targeting defenses, including Piwi-interacting (pi)RNAs, retrotransposon LINE-1 (L1) still thrives in humans and mice. To gain insights into L1 endurance, we characterized L1 Bodies (LBs) and ORF1p complexes in germ cells of piRNA-deficient *Maelstrom* null mice. We report that ORF1p interacts with TE RNAs, genic mRNAs, and stress granule proteins, consistent with earlier studies. We also show that ORF1p associates with the CCR4-NOT deadenylation complex and PRKRA, a Protein Kinase R factor. Despite ORF1p interactions with these negative regulators of RNA expression, the stability and translation of LB-localized mRNAs remain unchanged. To scrutinize these findings, we studied the effects of PRKRA on L1 in cultured cells and showed that it elevates ORF1p levels and L1 retrotransposition. These results suggest that ORF1p-driven condensates promote L1 propagation, without affecting the metabolism of endogenous RNAs.

Keywords

Retrotransposition, retrotransposon LINE-1, germ cell, mouse, translation, RNA granule, meiosis

Introduction

Transposable elements (TEs) are discrete DNA sequences that can spread throughout the host genome [1,2]. TE mobilization fuels the evolution of genomes and reprograms gene expression regulatory networks [3-5]. However, TE insertions also mutate genes, perturb gene expression and disrupt genome integrity [6-8]. Previous studies have revealed the existence of defensive mechanisms aimed at reducing the destructive potential of TEs. Among these are DNA methylation [9,10], repressive histone modifications [11], small Piwi-interacting (pi)RNAs [12,13] and repressive Kruppel-associated box-containing zinc-finger proteins (KRAB-ZFP) [14-17]. Despite the long evolutionary history of TE-targeting mechanisms [9,18], most eukaryotic genomes, including human and rodent genomes, still harbor active TEs [19-22]. How TEs resist and adapt to constant pressure from hosts is a fascinating question deserving further analysis [23]. Prior studies revealed a few examples of arms races between TEs and their hosts, including mutations and deletions of KRAB-ZFP binding sites from regulatory sequences of target TEs [15,23,24]. Unlike viruses, however, TEs rarely encode active countermeasures allowing to escape the defensive mechanisms of the host [23]. In particular, no such mechanisms have been reported for TEs active in animal genomes.

To better understand the interactions of TEs with their hosts in mammals, we focus on retrotransposon **L**ong **In**terspersed **E**lement-1 (LINE-1 or L1) [25]. L1 sequences are highly abundant in mammalian genomes accounting for 17.4% of human and 19% of mouse genomes [26,27]. Crucially, both genomes possess intact L1 copies capable of retrotransposition [20-22]. Indeed, an ongoing L1 activity is evident in the human population, with 124 L1-mediated disease-causing mutations identified so far [7]. Likewise, L1 insertions account for over 10% of novel germline mutations in mice [19,28]. The L1 life cycle involves the transcription and translation of L1 RNA, producing the RNA-binding protein ORF1p and the endonuclease/reverse transcriptase ORF2p [8,25,29]. The two proteins bind L1 RNA forming a ribonucleoprotein particle (RNP) [30,31]. Once L1

RNP enters the nucleus, ORF2p uses its two activities to execute target-primed reverse transcription (TPRT), generating a new L1 copy [32,33].

Much of the current understanding of L1 comes from studies in cultured mammalian cells ectopically overexpressing L1. This approach bypasses L1 repression, allowing mechanistic studies and quantification of L1 retrotransposition [34-36]. Furthermore, epitope tagging of L1 proteins allows the visualization of their subcellular distribution and the characterization of isolated L1 RNPs [37-41]. For example, prior studies documented the preferential localization of ORF1p to stress granules (SGs), RNA-containing biocondensates that appear upon cell exposure to various stresses [42-44].

The discovery of a germ cell defensive piRNA pathway extended systematic TE studies to various animal species. This adaptive immunity protects germ cells and their genomes from TEs [12,13]. Critically, because piRNAs function predominantly in germ cells, genetic perturbations of the piRNA pathway render mutant animals sterile but viable. One conserved piRNA factor is *Maelstrom* (*Mael*), which encodes an RNA-binding protein required for piRNA biogenesis [45-49]. Male germ cells of *Mael*$^{-/-}$ mice express high levels of L1, making them an ideal model to characterize the consequences of L1 overexpression [46]. In our prior studies, we characterized *Mael* expression and examined the impact of L1 overexpression on germ cells [46,50,51]. We also used L1 ORF1p overexpression in the *Mael* mutant to discover novel features of germ cell differentiation in both sexes [52-54]. This work focused on cytoplasmic aggregates highly enriched in ORF1p that form in *Mael*$^{-/-}$ male germ cells. Using a combination of approaches, we investigated the macromolecular composition of ORF1p complexes and revealed a mechanism that allows L1 to evade post-transcriptional repression.

Results

Mael$^{-/-}$ spermatocytes develop cytoplasmic bodies enriched in ORF1p, L1 RNA, and ribosomes

Meiotic male germ cells (spermatocytes) of *Mael*$^{-/-}$ mice overexpress L1 and develop prominent ORF1p-positive cytoplasmic bodies packed with ~25 nm electron-dense particles [46]. This work will refer to these structures as LBs for **L**INE-1 **B**odies. In EM images, LBs first appear as submicron cytoplasmic aggregates (Figure 1A, 1B, 1A' and 1B'), reminiscent of ORF1p aggregates occurring in wild-type (WT) spermatocytes (Figure S1). In *Mael*$^{-/-}$ mice, smaller LBs appear to fuse, forming large LBs that sometimes associate with membranes (Figure 1C - 1E). LBs reach 3 µm in size, exceeding the maximum sizes reported for Stress Granules (SGs, 2 µm) and Processing Bodies (p-bodies or PBs, 0.5 µm) [55,56]. A 3D reconstruction of LBs, using multiple z-plane confocal images of ORF1p signal in *Mael*$^{-/-}$ spermatocytes, revealed that LBs occupy large cytoplasmic volumes while embracing the nuclei (Figure 1F).

We next asked if electron-dense particles comprising LBs corresponded to L1 RNPs [57], ribosomes, or both. Previously, we used immunogold-EM to confirm the predominant ORF1p localization to LBs [46]. To verify L1 RNA enrichment in LBs, we performed sequential L1 ORF1p immunofluorescence followed by Hybridization Chain Reaction (HCR) RNA FISH using L1 DNA probes [58]. We observed robust L1 RNA signals that colocalized with L1 ORF1p in LBs of *Mael*$^{-/-}$ spermatocytes (Figure 1G). Control spermatocytes sporadically have cytoplasmic L1 RNA and ORF1p-positive granules similar to early LBs (Figures 1A', 1G, and S1).

To assess the ribosomal content of LBs, we examined the subcellular localization of RPS6 and RPL28 proteins of small and large ribosomal subunits, respectively. Immunofluorescence analysis revealed the abundant and uniform distribution of the two tested ribosomal proteins

throughout individual LBs (Figure 1H). The above findings suggest that LBs are large cytoplasmic compartments enriched in L1 RNA, ORF1p, and ribosomes. Although LBs might be cytoplasmic RNA granules, they are distinct from SGs and PBs that lack ribosomes [59].

L1-polysome and L1 RNP complexes in *Mael*$^{-/-}$ testes

To investigate L1 RNA and ORF1p association with ribosomes, we fractionated *Mael*$^{-/-}$ and *Mael*$^{+/-}$ testicular extracts through 10-50% linear sucrose gradients. We collected twelve fractions per gradient from the top (fraction 1) to the bottom (fraction 12) and analyzed the distributions of proteins and RNAs by Western blot and quantitative RT-PCR, respectively. In one set of experiments, we added cycloheximide (CHX) to samples to prevent ribosome runoff. We validated the resulting gradients by monitoring the 254 nm UV absorbance profile to reveal the characteristic peaks corresponding to 40S and 60S ribosomal subunits, 80S ribosomes, and polysomes (Figure 2A). Western blot analysis of ribosomal protein RPS6 confirmed the ribosome distribution in the gradient. At the same time, all gradient fractions contained ORF1p but with a clear enrichment in polysome-containing fractions toward the bottom of the gradient (Figure 2A). Importantly, qRT-PCR analysis of L1 RNA using *ORF1* amplicon showed a corresponding broad distribution pattern but with a peak in early polysomal fractions 6-8 (Figure 2B). The control beta-actin (*Actb*) mRNA's sedimentation profile confirmed the efficiency of the CHX treatment. Consistent with previous studies [57,60,61], the observed L1 RNA gradient pattern suggests the existence of L1 ribonucleoprotein (RNP) complexes distinct from ribosome-L1 RNA associations.

To assess how the association with ribosomes influences ORF1p and L1 RNA sedimentation, we fractionated *Mael*$^{-/-}$ testicular extracts in the presence of 10 mM EDTA, causing ribosome dissociation. Indeed, both the UV absorbance profile (Figure 2C, in blue) and the RPS6 sedimentation behavior showed robust changes following EDTA treatment of the sample (Figure 2C, + EDTA). In contrast, ORF1p showed only modest changes in its distribution across the

gradient (Figure 2C, + EDTA) compared to the previously described cycloheximide treatment. Furthermore, while *Actb* mRNA exhibited the expected shift from polysomes to lighter fractions, L1 RNA showed enrichment in the same region where ORF1p sediments (Figure 2D, fractions 5 - 8). These results further suggest the existence of a population of L1 RNA- and ORF1p-containing complexes independent from ribosomes. Finally, dual RNase A/T1 digestion of EDTA-treated samples disrupted such L1 complexes (Figure 2C, + EDTA + RNase), confirming the central role of RNA in generating the ORF1p pattern in presumptive RNP regions of the gradient. These data suggest that the cellular pool of L1 RNA and ORF1p comprises ribosome-independent and ribosome-associated complexes. The former might correspond to assembled L1 RNPs, while the latter could be the translating L1 polysomes.

L1 ORF1p associates with L1, other TE and genic mRNAs

To characterize ORF1p complexes, we first identified the RNA present in EDTA-resistant RNPs. We performed anti-ORF1p immunoprecipitation from pooled sucrose fractions 5 - 8, followed by RNA-seq of the precipitated material (Figures 2C and S2). Besides L1 RNA, non-autonomous retrotransposon RNAs and genic mRNAs can form RNPs with L1 proteins to re-enter the genome [37,62,63]. We therefore examined our RNA-seq data initially for genomic repeat RNAs and subsequently for genic mRNAs. We compared the RNA content of ORF1p immunoprecipitated (IP) samples to that of the unfractionated *Mael*$^{-/-}$ testis lysates (TOTAL), pooled fractions 5 - 8 (INPUT), or material bound non-specifically to carrier beads only (BO). We observed a strong enrichment of RNAs corresponding to evolutionarily young L1MdA and L1MdT families, which account for most full-length, intact L1 copies in the mouse genome (Figure 3A). Despite comparable levels in the TOTAL and INPUT samples, RNA of an evolutionarily older L1MdF2 family showed only minor enrichment in IPs. This observation further supports the notion that ORF1p and L1 RNA in fractions 5 - 8 form RNPs with a strong *cis*-preference for the coding L1 RNA, as reported previously [30,31].

RNA-seq analysis also revealed two unexpected features of germ-cell ORF1p complexes. First, in contrast to the established role of L1 in the mobilization of non-autonomous retrotransposons [64,65], we observed no enrichment for RNA of SINE B2 elements, despite their high abundance in the TOTAL (Figure 3A). Second, endogenous retrovirus MMERVK10C-int RNA showed strong enrichment in ORF1p complexes (Figure 3A). Nevertheless, numerous other TE RNAs did not enrich in ORF1p immunoprecipitates (Figure S3A).

Focusing on genic mRNAs, we identified 2081 transcripts associated with ORF1p (log2FoldChange > 1 and padj < 0.05 in IP vs. BO & IP vs. INPUT) (Figure 3B and Table S1). Of these, 1347 mRNAs were enriched over the TOTAL, consistent with their ORF1p association (Figure 3B and 3C, in red). The remaining 734 mRNAs (shown in grey and blue in Figure 3C) did not show enrichment over the TOTAL. Among them, a small group of "depleted" mRNAs (n=18; Figure 3C, in blue) showed higher levels in *Mael*$^{-/-}$ testis extracts (x-axis, TOTAL) than in ORF1p immunoprecipitates (y-axis, IP).

To gain insight into mRNA-ORF1p associations, we examined the relationships between the abundance of mRNAs in ORF1p complexes and their expression levels and lengths. mRNA expression levels correlated strongly with the probability of associating with ORF1p (R^2 = 0.844, p = 0; Figure 3C). Prior studies showed that mRNAs enriched in cytoplasmic granules are longer than an average transcript [44,66]. However, no such correlation is apparent for ORF1p-associated mRNAs (Figure 3D), further highlighting the difference between LBs versus SGs and PBs. The simplest explanation of these results is that an individual mRNA expression level is the primary determinant of their association with ORF1p. We also tested if enriched mRNAs (n=1347) belonged to a functionally focused subset of the germ cell transcriptome. Although Gene Ontology

analysis revealed the expected over-representation of germ cell and cell cycle mRNAs, no functional categories appeared to dominate (Figure S3B and Table S2).

To verify the localization of ORF1p-associated RNAs in LBs, we performed an HCR RNA FISH of *MMERVK10c-int* and *Setx* mRNAs. We observed the colocalization of both mRNAs with L1 RNA in LBs (Figure 3E). In control *Mael*$^{+/-}$ samples, both mRNA species showed a diffuse dotted pattern. Additional negative (RNase A treatment before hybridization) and positive (U6 small nuclear RNA hybridization) controls for the RNA FISH experiments confirmed the specificity of the detection (Figure S4). These results strongly support our RNA-seq findings and confirm the capability of ORF1p to bind to RNAs independently of their functionality or length and amass them in LBs.

ORF1p interacts with components of RNA granules, the CCR4-NOT complex, and ribosomes

To further characterize ORF1p interactions, we identified proteins co-immunoprecipitated with ORF1p from total *Mael*$^{-/-}$ testicular extracts using mass spectrometry. Two independent experiments detected 569 and 655 proteins, including ORF1p (Table S3). Upon filtering out low-specificity proteins (see Materials and Methods and Table S3), we identified 80 high-confidence ORF1p interactors common to both datasets (Table S4). Of these, 36 are homologs of human proteins reported previously as putative ORF1p interactors (Table S5).

To better understand the ORF1p interactome, we used the STRING database (Search Tool for Recurring Instances of Neighboring Genes, https://string-db.org/) to generate protein networks [67]. This analysis showed that ORF1p interactors common between previous studies and this work (Figure 4, “known”) fell into cytoplasmic "RNA granules" and "Ribosome" networks. The "RNA granules" network includes, among others, LARP1, G3PB2, MOV10, DDX6, FMR1, YBX1,

ELAV1, and PABPC1 proteins. Many of these proteins are exclusive for SGs, known to harbor ORF1p upon L1 overexpression in cultured cells [42,59]. Newly discovered ORF1p interactors associated with the same network include CAPRIN1 and FMR1-related FXR1 and FXR2 proteins, further strengthening the view of ORF1p association with SGs [68]. Newly discovered ORF1p interactors also included several proteins of the CCR4-NOT complex, a global regulator of mRNA metabolism frequently recruited to PBs [69,70]. Among the ORF1p-associated CCR4-NOT proteins, we consistently detected catalytic CNOT6L and CNOT7 proteins involved in mRNA deadenylation but not the scaffold CNOT1 protein and CNOT4 E3 ubiquitin ligase. The "Ribosome" network comprised proteins of both ribosomal subunits. Seven of eleven previously identified [37] and six newly discovered ORF1p-associated ribosomal proteins are components of the 60S subunit. This finding suggests that LBs are distinct from SGs, which contain the small (40S) but not large (60S) ribosomal subunits, and PBs, devoid of ribosomes altogether [43].

To determine the RNA-dependency of ORF1p interactions, we treated *Mael*$^{-/-}$ testis extracts with an RNase cocktail before immunoprecipitation (Figure S5A and S5B). The RNase treatment allowed for a better recovery of the bait protein ORF1p compared to an untreated sample (Figure S5C). This result can be explained by the removal of physical hindrance around ORF1p caused by RNA and RNA-dependent interactors. ORF1p association with most RNA granule components and the CCR4-NOT complex is strongly reduced or completely lost upon RNase treatment (Table S4). In contrast, RNase treatment did not significantly affect the interactions of ORF1p with ribosomal proteins, despite the compromised integrity of rRNA and ribosomes (Figures 4, S5D and Table S4).

We next performed double immunofluorescence labeling of testicular sections to support further the identified ORF1p interactions with RNA granules proteins and the CCR4-NOT complex. We established the colocalization of RNA helicase DDX6, enriched in both PBs and SGs, and

CNOT7, one of two deadenylase subunits of the CCR4-NOT complex, with ORF1p (Figure 5). DDX6 localized to cytoplasmic punctate foci in both spermatogonia and in control and ORF1p-negative *Mael*-mutant spermatocytes (Figure 5A, yellow arrows). However, DDX6 clearly redistributed to LBs whenever present in the cytoplasm of *Mael*$^{-/-}$ spermatocytes (Figure 5A, white arrowheads). CNOT7 shows a similar staining pattern, characterized by the formation of prominent cytoplasmic foci in the WT (Figure 5B, yellow arrows) and the aggregation with ORF1p in *Mael*$^{-/-}$ spermatocytes (Figure 5B, white arrowheads). We also asked if CNOT1, a scaffold protein essential for the CCR4-NOT complex assembly, localized to LBs along with ORF1p. Although absent among ORF1p interactors, we detected CNOT1 in LBs (Figure S6A, white arrowheads). Finally, given the frequent association of CCR4-NOT with PBs, we asked if LBs contained other PB proteins, such as DCP1A. Interestingly, in contrast to the abundance of DCP1A in PBs of various sizes in control samples, DCP1A appears mostly confined to prominent granules with strong signals at the periphery of *Mael*$^{-/-}$ seminiferous tubules (Figures 5C and S6B). Sporadically, we also observed weak diffused DCP1A staining in LBs (Figure 5C, white arrowheads). This observation suggests that L1 overexpression and LBs formation disrupt PBs formation. Cumulatively these results demonstrate that LBs are unusual hybrid cytoplasmic compartments bearing characteristics of SGs and perhaps PBs and yet enriched in ribosomes.

ORF1p binding does not affect the stability and translation efficiency of mRNAs

The above findings raise an important question about the impact of LBs on RNA stability and translation. To test if ORF1p-associated RNAs exhibit signs of 5' or 3' degradation, we examined the read coverage across all RNAs detected in ORF1p immunoprecipitated EDTA-resistant RNPs (IP) and compared these results to the unfractionated *Mael*$^{-/-}$ testicular extracts (TOTAL). A reduction or lack of coverage towards the 5’ or the 3’ termini would be consistent with RNA degradation by resident SG and PB exonucleases. We computationally divided all detected mRNAs into ten bins, each corresponding to 10% of the total RNA length. We then calculated the

read coverage across each region for every RNA and the cumulative coverage across each region for all RNAs detected in IP vs. TOTAL samples (Figure 6A). We did not observe reduction of coverage at any of the ends for immunoprecipitated RNAs compared to total extracts (Figure 6A), suggesting that ORF1p-bound RNAs are intact.

To investigate if CCR4-NOT complex association with L1 ORF1p resulted in increased deadenylation of LB-localized mRNAs, we analyzed the poly(A) tail length of two ORF1p-associated mRNAs (*Sycp1* and *Setx*) in *Mael*$^{-/-}$ and control juvenile testes of comparable tissue complexity at postnatal day 16 (P16) (Figure 6B and 6C). Using a PCR-based approach, we found no significant differences in the poly(A) tail length of the tested mRNAs between *Mael*$^{-/-}$ and control littermates (Figure 6C). These findings suggest that the CCR4-NOT complex does not deadenylate LB-localized mRNAs.

To assess the impact of LB-localized RNA granule proteins on the translation of ORF1p-bound mRNAs, we performed ribosome profiling of *Mael*$^{-/-}$ and control P16 testes. As expected, this analysis showed low expression and ribosomal coverage of the mutated *Mael* mRNA in the *Mael*$^{-/-}$ sample (Figure 6D). In contrast, we found no evidence of significant disruption of translation efficiency in general and including ORF1p-associated mRNAs (ORF1p-bound, n=1313) (Figure 6D).

To further investigate the translational status of P16 testes, we tested the eIF2α phosphorylation level in *Mael*$^{+/-}$ and *Mael*$^{-/-}$ littermates (Figure 6E). Phosphorylation of translation initiation factor eIF2α ultimately causes inhibition of translation. In agreement with our ribo-footprint data, we found no significant difference in phospho-eIF2α levels between *Mael*$^{-/-}$ and *Mael*$^{+/-}$ testes (Figure 6E), consistently with an unperturbed translation. Collectively these data

show that the ability of ORF1p to amass endogenous mRNAs to LBs does not affect their stability or translation efficiency.

L1 coopts PRKRA to enhance ORF1p levels and retrotransposition

The above data suggest that despite numerous negative regulators of RNA expression in LBs, ORF1p-associated mRNAs avoid translational repression, suggesting a counteracting mechanism(s). Of particular interest is an RNA-independent ORF1p interactor PRKRA (also known as RAX and PACT), a protein that activates Protein Kinase R (PKR) [71]. Once activated, PKR phosphorylates eIF2α, causing translation inhibition [72]. PRKRA can also repress PKR and prevent activation of eIF2α, thus enhancing gene expression at the translational level [73,74]. In light of these opposing PRKRA activities, we asked which PRKRA-dependent mechanism operates in L1-overexpressing spermatocytes.

We first validated our earlier mass spectrometry findings by detecting PRKRA in the ORF1p immunoprecipitates from untreated and RNase-treated *Mael*$^{-/-}$ testicular lysates (Figure 7A). We also showed PRKRA and ORF1p colocalization in LBs (Figures 7B and S7A). Next, to test for PRKRA involvement in the L1 lifecycle, we generated a plasmid with an EF-1α promoter driving the expression of an mRNA encoding a 3XFLAG N-terminally tagged mouse PRKRA followed by P2A peptide and EGFP (pPRKRA; Figure S7B). We used a plasmid bearing the EGFP reporter as a negative control (pEGFP). To test if ectopic PRKRA interferes with endogenous L1 expression, we transfected 3XFLAG-tagged PRKRA into F9 cells expressing high levels of endogenous L1 elements. Ectopic PRKRA protein was detected by both anti-FLAG and anti-PRKRA antibodies with overlapping signals at the expected molecular weight; however, endogenous ORF1p expression remained unperturbed (Figure S7C). Finally, endogenous ORF1p interacted and co-localized with the PRKRA protein expressed ectopically in F9 cells (Figure S7D and S7E).

To test for the PRKRA effect on L1 mobilization, we performed L1 retrotransposition assays in human HeLa cells following the established protocol [34]. We transfected HeLa cells to co-express mouse PRKRA with a wild-type native mouse L1spa element (pTN201) [20]. To monitor the cytotoxicity of PRKRA overexpression, we co-transfected pPRKRA with a control reporter plasmid (pPAGFP-C1) containing the same selection marker (*neo*) as the L1 retrotransposition plasmid (Figure 7C) [34]. We used the resulting values in the reporter control assay to correct L1 plasmid retrotransposition frequencies in the presence of pEGFP or pPRKRA (see Materials and Methods for details). Retrotransposition frequencies observed in the presence of the control plasmid (pEGFP) in place of pPRKRA were considered the baseline. Figures 7C and 7D demonstrate that PRKRA can enhance the retrotransposition efficiency of a mouse L1spa element in HeLa cells compared to the control. To confirm that L1 retrotransposition in the presence of pPRKRA proceeds according to the established mechanism, we used plasmids expressing a synthetic mouse wild-type and catalytically inactive L1 elements (Figure S7F) [20,75]. To gain insight into the PRKRA mechanism of action in L1 retrotransposition, we measured mouse L1 RNA and ORF1p levels in HeLa cells co-transfected with L1spa and pPRKRA. While L1spa RNA levels decreased by 25% (Figure 7E), its ORF1p levels increased in the presence of PRKRA (Figure 7F and 7G) compared to controls (pEGFP empty vector). Finally, we observed a moderate reduction of eIF2α phosphorylation upon expression of pPRKRA and L1spa in HeLa cells compared to controls (Figure 7H and 7I), consistent with the increase of L1spa ORF1p levels described above (Figure 7F and 7G).

Discussion

In contrast to the growing understanding of defenses protecting cells and their genomes from mobile DNA, mechanisms of TE endurance remain largely unexplored. In this work, we used an *in vivo* mouse model to characterize L1 interactome in germ cells, the most coveted cell lineage for TE expansion. Prior studies have examined L1 in cultured cells revealing the impressive complexity of L1 interactome (Table S5) [16,37-40,42]. This work demonstrates the conservation of the fundamental principle of L1 association with the multitude of RNA species and RNA granules proteins and offers new insights into ORF1p interactions with host factors.

Our results demonstrate that germ cells overexpressing L1 develop cytoplasmic bodies enriched for ORF1p, a subset of SG, some PB proteins, and the major cytoplasmic deadenylation complex CCR4-NOT. Immunofluorescence and immunogold labeling show that ORF1p accumulates in LBs at exceptionally high levels (this work and [46]). Prior studies in cultured cells have reported L1 association with SGs and their contribution to cellular defenses against L1 [17,37,38,76-78]. Meanwhile, L1 localization to PBs was reported only sporadically [79]. Although LBs harbor numerous RNA granule proteins, particularly those of SGs, we found that LBs contain proteins of both ribosomal subunits. In contrast, SGs and PBs lack fully assembled ribosomes [43,80]. Consistent with ribosome presence in LBs, a significant share of the cellular ORF1p co-sediments with polysomes in sucrose gradients. Ribosomes might account for the distinctive appearance of LBs in EM images accentuated by ~25 nm particles, reported neither for SGs nor PBs [81]. LBs are also significantly larger than SGs and PBs and frequently associate with double membranes. Because of the presence of ribosomes, LBs might be structurally or functionally related to neuronal RNA granules [82-84]. Indeed, besides ribosomes, LBs and neuronal granules share several other proteins, including G3BP2, CAPRIN1, FMR1, FXR1, FXR2, ELAV1, ELAV2, PURA, and others [82]. Nonetheless, LBs also differ from neuronal RNA granules, including their sizes and EM appearance, the lack of heavy RNA complexes below polysomes in sucrose

gradients, and the association eIF4A and eIF4E proteins with ORF1p. Thus, LBs are hybrid organelles harboring ORF1p, numerous RNA granule proteins, and ribosomes.

Our data suggest that L1 RNA and ORF1p are crucial for LBs assembly. There is a strong correlation between the increased L1 expression levels and the formation of LBs during meiotic prophase I ([46] and this study). Indeed, *Mael*$^{-/-}$ mice on the 129SvJae genetic background (as opposed to B6 used in this work) express lower ORF1p levels and form LBs less frequently [51]. Furthermore, small LB precursors are evident in wild-type germ cells expressing low levels of L1 in early meiosis (this work and [52]).

Our data also suggest that ORF1p drives LB assembly by interacting with RNAs and thus attracting numerous RNA-binding proteins. Consistent with prior findings [30,31], ORF1p shows a preference for RNA of evolutionarily young L1MdT and L1MdA elements. Unexpectedly, we observed no enrichment for SINE RNA, known to be mobilized by the L1 machinery [64,65,85,86], and strong enrichment for MMERVK10C-int RNA [87]. We also found that ORF1p is associated with numerous genic mRNAs, and such interactions correlate with mRNA expression levels. These observations agree with the evidence of the non-essential role of ORF1p in SINE retrotransposition but its requirement for generating processed pseudogenes [65,88]. Interestingly, the pool of heterogeneous RNAs associating with ORF1p shares the capacity for translation. Considering that ORF1p interacts with ribosomes, as shown by orthogonal approaches, we propose that ORF1p might interact with ribosome-associated RNAs. Notably, our observations *in vivo* agree with recent reports of ORF1p capacity to phase separate and form condensates with RNAs that are required for L1 retrotransposition, further supporting the leading role of ORF1p in LBs formation [89,90].

Prior studies proposed that L1 RNP localization to SGs might restrict L1 activity as a defense mechanism [42]. Indeed, the colocalization and RNA-mediated interactions of ORF1p with various RNA granule proteins identified in this study might suggest that LBs are sites of RNA storage, destabilization, or translational repression. However, a paradoxical feature of LBs is that despite numerous proteins implicated in RNA regulation, we find no evidence of reduced RNA stability and translation. For example, although the CCR4-NOT complex is a major deadenylase, we did not observe augmented deadenylation of ORF1p-associated RNAs. These observations suggest that the CCR4-NOT complex might be inactivated in the context of LBs by other factors, such as shown for RNF219 E3-ubiquitin ligase [91]. Alternatively, the CCR4-NOT complex might perform a different function in LBs, such as facilitating the co-translational assembly of ORF1p trimers, which must rapidly oligomerize to ensure L1 retrotransposition [92]. This idea reflects a previously established role of CCR4-NOT in the assembly of the proteasome, RNA Polymerase II, and the SAGA complex [93-95]. Furthermore, LBs contain ribosomes, and ORF1p interacts with ribosomal proteins following the stringent RNase treatment. Indeed, we did not detect reduced translation of mRNAs bound by ORF1p and the transcriptome in general. This result can be explained by the relocalization of only a minor fraction of germ cell mRNAs to LBs, rendering any translational changes difficult to detect overall. Alternatively, LBs might represent sites of active translation rather than mRNA storage or degradation. In agreement with this hypothesis, *Setx*, the most enriched mRNA in ORF1p complexes localizes to LBs and shows no reduction in translational efficiency or signs of deadenylation.

Further support for the above hypothesis comes from the evidence of ORF1p adapting PRKRA, a PKR factor, to prevent the activation of a crucial arm of the integrated stress response. Although under some conditions PRKRA (or its human homolog PACT/RAX) inhibits PKR [71,74,96,97], it primarily functions as a PKR activator, even in the absence of dsRNA [98]. Our data suggest that ORF1p-PKRKA interactions preclude PKR activation, phosphorylation of eIF2α, and

translational inhibition. Such negative control could happen either through ORF1p sequestering PRKRA and preventing it from activating PKR, or actively inducing PRKRA to inhibit PKR. ORF1p might fulfill the role of TRBP/TARBP2 protein that prevents PKR activation by heterodimerizing with PRKRA [97]. Under stress the TRBP-PRKRA complex disassembles, allowing PRKRA to activate PKR. ORF1p may bind the released PRKRA, thus preventing PKR activation and translational inhibition. In support of this hypothesis, ORF1p complexes characterized in this study contained only small amounts of TARBP2 compared to PRKRA, suggesting a preferential binding of ORF1p to PRKRA in place of TARBP2. Notably, PKR is dispensable for L1 RNP localization to SGs in cultured cells devoid of three major eIF2α activating kinases, including PKR [42]. Furthermore, we observed enhancement of L1spa retrotransposition in HeLa cells upon PRKRA overexpression. This effect can be partially explained by the increase in ORF1p levels in the presence of PRKRA, possibly facilitating L1 mobilization. Further experiments will be needed to address the mechanism of ORF1p augmentation, which can happen either at the translational level through a PRKRA-mediated translational stimulation, or post-translation through protein stabilization.

Taken together our data suggest that - like viruses - L1 encodes an active mechanism that counteracts cellular defenses. Viruses have evolved many countermeasures to overcome translational inhibition [99]. A particularly successful strategy employed by viruses is to inhibit the initiation of cap-dependent translation. This strategy allows viruses to attract ribosomes to viral RNAs and increase translation initiation via Internal Ribosomal Entry Site elements. The strategy, however, is likely unfavorable for TEs since the host's fitness ensures TE propagation [23]. Therefore, the proposed mechanism of relieving translational inhibition could be the optimal solution that satisfies the needs of L1 and the host.

To conclude, this study revealed the formation of a novel cytoplasmic RNA body upon L1 overexpression in mouse germ cells. LBs are hybrid structures, harboring RNA metabolism and translational repression proteins and ribosomes. Despite the nucleation of LBs, no successful containment of L1 occurs, and the stability and translation efficiency of cellular RNAs are not compromised. In addition, L1 appears to evade cellular defenses and translational shut-off by co-opting the PKR-associated protein PRKRA. In this manner, L1 increases its chances of further spreading in the host genome and fueling genomic diversity. We speculate that the described mechanism might be of particular significance in somatic cells lacking piRNAs naturally and might account for the emerging roles of L1 in aging and disease [100-103]. Additional studies will provide deeper mechanistic insights into LBs functions and L1-PRKRA/PKR interactions.

Acknowledgements

We thank Allison Pinder, Dr. Fred Tan, Dr. Xiaobin Zheng and Dr. Sarah Wheelan for assistance with sequencing and data analyses; Dr. Eugenia Dikovsky and the Animal Facility staff for assistance with animal care; Dr. Kamena Kostova for advice on ribosome profiling; Rejeanne Juste for assistance with genotyping and tissue sectioning; Dr. Svetlana Deryusheva for reagents and assistance with RNA FISH optimization; Dr. Mahmud Siddiqi for assistance with microscopy and automated colony counting in retrotransposition assays; Michael Sepanski for assistance with EM imaging. We thank Dr. Joseph Tran, Dr. Zhao "ZZ" Zhang and past and present members of the Bortvin lab for discussions and suggestions. We thank Dr. John Goodier and Dr. Svetlana Deryusheva for their feedback on the manuscript. Funding: Carnegie Institution for Science endowment (C.D.L. and A.B.) and National Institutes of Health grant R21HG010512 (A.B.).

Author contributions

Conceptualization, C.D.L. and A.B.; Data curation, C.D.L. and A.G.; Formal analysis, C.D.L.; Funding acquisition, A.B.; Investigation, C.D.L. and A.B.; Methodology, C.D.L. and A.B.; Project administration, A.B.; Resources, A.B.; Software, C.D.L. and A.G.; Supervision, A.B.; Validation,

C.D.L.; Visualization, C.D.L. and A.B.; Writing – original draft, C.D.L. and A.B.; Writing – review & editing, C.D.L. and A.B.

Declaration of interests

The authors declare no competing interests

Inclusion and diversity

We support inclusive, diverse, and equitable conduct of research.

Data and code availability

• The sequencing data discussed in this publication have been deposited in NCBI's Gene Expression Omnibus [104] and are accessible through GEO Series accession numbers GSE222415 (https://www.ncbi.nlm.nih.gov/geo/query/acc.cgi?acc=GSE222415) and GSE222416 (https://www.ncbi.nlm.nih.gov/geo/query/acc.cgi?acc=GSE222416).

• The mass spectrometry datasets discussed in this publication are available from ProteomeXchange.

• Original code is available at Carnegie Embryology GitHub (https://github.com/ciwemb/bortvin-2023-orf1p).

• Any additional information required to reanalyze the data reported in this paper is available from the lead contact upon request.

Figure 1. L1 bodies (LBs) are large cytoplasmic compartments enriched in ORF1p, L1 mRNA, and ribosomes. (A – E) Electron micrographs exemplifying the formation of LBs in *Mael*$^{-/-}$ spermatocytes. Boxed areas in A and B identify small cytoplasmic aggregates magnified in A' and B', respectively. Boxed area in C identifies an intermediate size LB magnified in C'. D and E show more prominent LBs, partially surrounded by a bilayer membrane (red arrows). NE: nuclear envelope. **(F)** Immunofluorescence staining of L1 ORF1p on *Mael*$^{-/-}$ spermatocytes shows ORF1p accumulation in LBs (left panel, magenta). 3D reconstruction of LBs (magenta) and nuclei (blue) (middle and right panels); numbers (1-5) are used to label corresponding cells. Scale bars: 5 µm. **(G)** HCR RNA-FISH of L1 RNA (green) and immunofluorescence staining of L1 ORF1p (magenta) on *Mael*$^{+/-}$ and *Mael*$^{-/-}$ testis sections. Scale bars: 5 µm. **(H)** Double immunofluorescence staining of ribosomal protein S6 (RPS6, top two rows, green) or L28 (RPL28, bottom two rows, green) and L1 ORF1p (magenta) showing their colocalization in LBs. Dotted white lines mark seminiferous tubule boundaries. Scale bars: 15 µm. See also Figure S1.

Figure 2. L1-polysome and L1 RNP complexes in *Mael*$^{-/-}$ testes. (A) Western blot analysis of L1 ORF1p and RPS6 in *Mael*$^{-/-}$ testicular extracts fractionated through 10-50% sucrose gradients in the presence of cycloheximide (CHX). Fractionated *Mael*$^{+/-}$ extract served as a negative control. The absorbance profile of the gradient is shown in red. **(B)** qRT-PCR analysis of L1 RNA (L1 ORF1 amplicon) and beta-actin mRNA (Actb) in *Mael*$^{-/-}$ testicular extracts fractionated through 10-50% sucrose gradients in the presence of CHX. RNA amounts per fraction are reported as percentages of the total RNA detected across the gradient; barplot shows mean percentage values + SEM of four biological replicates. **(C)** Western blot analysis of L1 ORF1p and RPS6 in *Mael*$^{-/-}$ testicular extracts fractionated through 10-50% sucrose gradients in the presence of EDTA (+ EDTA); the absorbance profile of the gradient is shown in blue. Upon addition of RNases A and T1 (+ EDTA + RNase) ribosomes are degraded (profile in green) and L1 RNPs disaggregated. **(D)** qRT-PCR analysis of L1 RNA (L1 ORF1 amplicon) and beta-actin mRNA (Actb) in *Mael*$^{-/-}$

testicular extracts fractionated through 10-50% sucrose gradients in the presence of EDTA. Barplot shows mean percentage values + SEM of three biological replicates. See also Figure S2.

Figure 3. L1 ORF1p binds to L1, other TEs and abundant genic mRNAs. (A) RNA levels of selected genomic repeats across anti-ORF1p co-immunoprecipitation samples (IP, TOTAL, Beads Only (BO), INPUT; in triplicate). Heatmap reports log2 normalized collapsed read counts; color indicates RNA levels. **(B)** Identification of mRNAs bound by L1 ORF1p in IP samples (n=2081). For every comparison (IP vs. BO, IP vs. TOTAL or IP vs. INPUT), mRNAs with log2FoldChange > 1 and padj < 0.05 were considered enriched. **(C)** Linear regression analysis of n=2081 ORF1p-bound mRNAs showing the relationship between their expression level in *Mael*$^{-/-}$ testes (x axis, TOTAL) and their enrichment in L1 RNPs (y axis, IP). Scatterplot shows log2 mean normalized counts. **(D)** Linear regression analysis of n=2081 ORF1p-bound mRNAs showing the relationship between their length (x axis, log2 length in nucleotides) and their enrichment in L1 RNPs (y axis, IP). **(E)** Multiplexed HCR RNA-FISH of MMERVK10c-int and Setx with L1 RNA on *Mael*$^{+/-}$ and *Mael*$^{-/-}$ testis sections. Images of spermatocytes and round spermatids are reported. Scale bars: 5 µm. See also Figures S3 and S4.

Figure 4. L1 ORF1p associates with cytoplasmic RNA granules components, the CCR4-NOT complex and ribosomal proteins. Network of physical and functional interactions among the 80 high-confidence L1 ORF1p interactors identified in this study. The network was generated using the STRING database; thickness of connection lines indicates the strength of data support. Proteins identified for the first time in this work (new) are marked in blue, while previously known ORF1p interactors are marked in green. ORF1p interactors resistant to RNase treatment are enclosed in dashed grey areas. *: unspecific interactor. See also Figure S5.

Figure 5. LBs are enriched with DDX6 and CNOT7 proteins. (A) Double immunofluorescence staining of RNA helicase DDX6 (green) and L1 ORF1p (magenta) in *Mael*$^{+/-}$ and *Mael*$^{-/-}$ testes. DDX6 is detectable in cytoplasmic foci in both *Mael*$^{+/-}$ and *Mael*$^{-/-}$ spermatogonia and spermatocytes (yellow arrows); in *Mael*$^{-/-}$ both ORF1p and DDX6 concentrate in LBs (white arrowheads). Dotted white lines mark seminiferous tubule boundaries. Scale bars: 10 µm. **(B)** Double immunofluorescence staining of CCR4-NOT complex subunit CNOT7 (green) and L1 ORF1p (magenta) in *Mael*$^{+/+}$ and *Mael*$^{-/-}$ testes. CNOT7 is detectable in cytoplasmic foci in *Mael*$^{+/+}$ spermatocytes (yellow arrows); in *Mael*$^{-/-}$ CNOT7 colocalizes with ORF1p in LBs (white arrowheads). Scale bars: 10 µm. **(C)** Double immunofluorescence staining of DCP1A (green) and L1 ORF1p (magenta) in *Mael*$^{+/-}$ and *Mael*$^{-/-}$ testes. DCP1A shows a characteristic granular pattern in both samples (yellow arrows), although PBs appear overall less abundant in *Mael*$^{-/-}$ seminiferous tubules; weak diffuse DCP1A signal is also detected in LBs (white arrowheads). Boxed areas in *Mael*$^{-/-}$ panels are magnified in insets. Scale bars: 10 µm. See also Figure S6.

Figure 6. L1 ORF1p binding to endogenous mRNAs affects neither their stability nor their translation efficiency. (A) RNA-seq coverage of RNAs detected in anti-L1 ORF1p co-immunoprecipitation samples (IP and TOTAL; shown in triplicate). Each of the segments on the x axis (labeled 1 to 10) corresponds to 10% of transcript lengths; the cumulative number of reads across each segment is plotted (y axis, read count x10^6). **(B)** Immunofluorescence staining of L1 ORF1p (magenta) in P16 *Mael*$^{+/-}$ and *Mael*$^{-/-}$ testes. Scale bars: 100 µm. **(C)** Analysis of the poly(A) tail of *Sycp1* and *Setx* mRNAs in P16 testes of *Mael*$^{+/-}$ and *Mael*$^{-/-}$ littermates. A schematic of the assay is shown on the left; numbers mark the assay steps: 1) poly(U) tailing; 2) cDNA synthesis using an RT adapter; and 3) PCR spanning the poly(A) tail. Representative gels are shown on the right; the assay was performed in biological triplicate. **(D)** Scatterplot showing the relationship between mRNA level changes (x axis, RNA-seq log2FoldChange) and ribo-footprint changes (y axis, Ribo-seq log2FoldChange) in *Mael*$^{-/-}$ over *Mael*$^{+/-}$ testes. A subset of 1313

mRNAs found associated with ORF1p previously in this study are labeled in red. ΔTE n.s.: difference in Translation Efficiency between *Mael*$^{-/-}$ and *Mael*$^{+/-}$ non significant. **(E)** Western blot analysis of phosphorylated eIF2α levels (P-eIF2α) in P16 testes of *Mael*$^{+/-}$ and *Mael*$^{-/-}$ littermates. Blot #1 and #2 were run and processed in parallel. Blot #1 was first probed with an anti-P-eIF2α antibody, then stripped and re-probed with an anti-eIF2α antibody (pan); blot #2 was probed sequentially with the monoclonal anti-ORF1p (Abcam) and an anti-DDX4/MVH antibody.

Figure 7. RNase-resistant ORF1p-interactor PRKRA localizes to LBs *in vivo* and promotes mouse L1 retrotransposition in cultured human cells. (A) Western blot analysis of PRKRA in anti-L1 ORF1p co-immunoprecipitation samples from *Mael*$^{-/-}$ testes. Immunoprecipitation with an isotype IgG was used as a negative control; note the higher yield of ORF1p in the presence of RNases. Super: supernatant. **(B)** Double immunofluorescence staining of PRKRA (green) and L1 ORF1p (magenta) in *Mael*$^{+/-}$ and *Mael*$^{-/-}$ testes shows PRKRA enrichment in LBs (yellow arrows). Scale bars: 10 μm. **(C)** Representative L1 retrotransposition assay results using the retrotransposition-competent or control plasmids listed on the left, in combination with pEGFP or pPRKRA in HeLa cells. neo^{R}: neomycin-resistant colonies. **(D)** Overexpression of mouse PRKRA stimulates retrotransposition of a mouse wild type L1. Box-and-whisker plot shows corrected retrotransposition efficiencies from five biological replicates. **(E)** qRT-PCR analysis of mouse L1 RNA (*ORF1* amplicon) derived from pTN201 co-transfected with pEGFP or pPRKRA in HeLa cells. Human *GAPDH* was used as the reference gene. Barplot shows relative normalized expression ± SEM of three biological replicates. Two-tailed unpaired Student's t-test: *** $p \leq 0.001$. **(F)** Western blot analysis of mouse ORF1p derived from pTN201 co-transfected with pEGFP or pPRKRA in HeLa cells. Alpha-tubulin (α-tub) serves as a loading control. **(G)** Barplot showing mean fold change of mouse ORF1p derived from pTN201 co-transfected with pPRKRA in HeLa cells. ORF1p band intensities are normalized to alpha-tubulin (α-tub) and further shown as fold change relative to control (pTN201 + pEGFP). Data are expressed as mean ± SEM of three

biological replicates. Two-tailed unpaired Student's t-test: ** $p \leq 0.01$. **(H)** Western blot analysis of human phosphorylated eIF2α (P-eIF2α) in the presence of pTN201 co-transfected with pEGFP or pPRKRA in HeLa cells. eIF2α (pan) serves as a loading control. **(I)** Barplot showing mean fold change of human P-eIF2α in the presence of pTN201 co-transfected with pPRKRA in HeLa cells. P-eIF2α band intensities are normalized to eIF2α and further shown as fold change relative to control (pTN201 + pEGFP). Data are expressed as mean ± SEM of three biological replicates. Two-tailed unpaired Student's t-test: * $p \leq 0.05$. See also Figure S7.

Supplemental Figure S1. L1 ORF1p aggregates can be detected in the cytoplasm of spermatocytes from BALB/c wild-type mice. (A) Immunofluorescence staining of L1 ORF1p (green) on BALB/c wild-type spermatocytes showing ORF1p accumulation in small cytoplasmic granules similar to early LBs. **(B – B')** Electron micrographs of a BALB/c wild-type spermatocyte harboring a small LB; boxed area in B is magnified in B'.

Supplemental Figure S2. L1 ORF1p can be efficiently pulled-down from either unfractionated testicular extracts or pools of sucrose fractions where L1 RNP complexes sediment. (A) Silver staining and **(B)** western blot analysis of anti-ORF1p immunoprecipitation samples (IP) from unfractionated and sucrose gradient fractionated (+ EDTA; pool sucrose fractions 5 - 8) *Mael*$^{-/-}$ testis extracts. Immunoprecipitations with carrier beads only (BO) were performed in parallel for background estimation; samples obtained from *Mael*$^{+/-}$ mice are shown as negative controls. Super: supernatant.

Supplemental Figure S3. Genomic repeats and mRNAs detected across anti-L1 ORF1p co-immunoprecipitation samples. (A) Extensive heatmap of repeat families detected across anti-L1 ORF1p co-immunoprecipitation samples: carrier beads only (BO), ORF1p immunoprecipitated samples (IP), pooled sucrose fractions 5 - 8 (INPUT), *Mael*$^{-/-}$ testis extracts (TOTAL). Average expression level of ancestral L1Lx family in TOTAL samples was chosen as the threshold to exclude any repeat with a lower expression from the reported heatmap. For simplicity, low complexity regions, rRNA, tRNA, satellites and simple repeats were also excluded. **(B)** Gene Ontology analysis (Biological Process) of the set of mRNAs (n=1347) that were found strongly enriched in IP samples. Barplot shows the 13 most representative enriched GO terms (y axis, Term), with the corresponding number of genes identified per term (x axis, Count). Bars are labeled based on the False Discovery Rate (FDR).

Supplemental Figure S4. Negative and positive controls for HCR RNA-FISH. (A) Multiplexed HCR RNA-FISH of MMERVK10c-int and Setx with L1 RNA on *Mael*$^{-/-}$ testis sections minus (-) and plus (+) RNase A treatment. The RNase treatment is shown as a negative control for effective probe-RNA recognition. Scale bars: 40 µm. **(B)** HCR RNA-FISH of U6 small nuclear RNA on *Mael*$^{+/-}$ and *Mael*$^{-/-}$ testes. U6 small nuclear RNA was chosen as a positive control for its high abundance and strict nuclear localization. As expected, U6 shows strong nuclear signals, independent from the *Mael* mutation. Scale bars: *Mael*$^{+/-}$ section: 20 µm; *Mael*$^{-/-}$ section: 10 µm.

Supplemental Figure S5. Optimization of RNase treatment of testis extracts before co-immunoprecipitation. (A) Non-denaturing RNA agarose gel showing multiple RNase treatment conditions (lanes 3-6, see box for details) or untreated BL/6 testis total RNA (lane 2) as a control; the treatment used in lane 5 was chosen for co-immunoprecipitation experiments. Approximately 2 µg of RNA were loaded on each lane. **(B)** Bioanalyzer traces of RNA samples corresponding to lanes 2 and 5 in panel A. RIN: RNA Integrity Number; scale from 1 (fully degraded) to 10 (intact). **(C)** Silver staining of anti-ORF1p co-immunoprecipitation samples (IP) from *Mael*$^{-/-}$ testicular extracts minus (-) and plus (+) the RNase treatment used for lane 5 in panel A. Immunoprecipitation with an isotype IgG served as a negative control; note that the RNase treatment increases immunoprecipitation of ORF1p. **(D)** Heatmap showing the recovery of ribosomal proteins in anti-ORF1p co-immunoprecipitation samples from *Mael*$^{-/-}$ testes, minus (-) and plus (+) the RNase treatment used for lane 5 in panel A. Color indicates protein levels; E2.n indicates Experiment 2.replicate n. The relative abundance of each protein in each eluate was obtained by mass spectrometry analysis and further adjusted by dividing the PSM counts by molecular weights (MW); for a sample-to-sample comparison, the obtained PSM / MW ratios were normalized to the ratio obtained for the bait (LORF1).

Supplemental Figure S6. Localization of CNOT1 and DCP1A proteins in mouse *Mael*$^{+/-}$ and *Mael*$^{-/-}$ testes. (A) Double immunofluorescence staining of CNOT1 (green) and L1 ORF1p (magenta) in *Mael*$^{+/-}$ and *Mael*$^{-/-}$ testes. In *Mael*$^{+/-}$, CNOT1 shows aggregation in characteristic round cytoplasmic structures in spermatocytes (top panels, yellow arrows) and in more restricted cytoplasmic areas in round spermatids (top panels, red arrows). Similar structures are also observed in spermatocytes of *Mael*$^{-/-}$ mice (bottom panels, yellow arrows), where L1 ORF1p is not detected, in addition to some CNOT1 aggregation in LBs (bottom panels, white arrowheads). Scale bars: 15 μm. **(B)** Double immunofluorescence staining of DCP1A (green) and L1 ORF1p (magenta) in *Mael*$^{+/-}$ and *Mael*$^{-/-}$ testis sections. DCP1A shows a cytoplasmic granular pattern that is detected in all spermatogenic cells of *Mael*$^{+/-}$ control testes (top panels); signal intensities and sizes of granules are variable. In *Mael*$^{-/-}$ tubules (bottom panels), DCP1A is mostly confined to prominent granules with strong signals in peripheral spermatogonia; weak diffuse DCP1A signal is observed in LBs. Scale bars: 15 μm.

Supplemental Figure S7. PRKRA association with L1 ORF1p is recapitulated in F9 mouse carcinoma cells using an exogenous construct. (A) Immunofluorescence staining of PRKRA (green) in *Mael*$^{-/-}$ testis. PRKRA shows diffuse cytoplasmic signals in both germ (spermatogonia and spermatocytes) and somatic (Sertoli) cells; PRKRA aggregation in LBs-resembling structures in spermatocytes is also detected (yellow arrows). Scale bar: 15 μm. **(B)** Schematic representation of the pPRKRA plasmid driving the expression of N-terminal 3XFLAG mouse PRKRA followed by the self-cleaving P2A peptide and an EGFP reporter, and its control empty vector pEGFP. **(C)** Western blot analysis of exogenous PRKRA and endogenous ORF1p in F9 cells transfected with pEGFP or pPRKRA. Exogenous PRKRA was detected by both an anti-PRKRA and an anti-FLAG antibody with overlapping signals (red and green, respectively; left blot) at the expected MW (~ 37 kDa); no detectable perturbation of endogenous ORF1p was observed upon PRKRA overexpression (right blot). cyt: cytoplasmic extract; nuc: nuclear extract.

(D) Double immunofluorescence staining of 3XFLAG-PRKRA (anti-FLAG antibody) and L1 ORF1p in F9 cells transfected with pEGFP or pPRKRA. Boxed areas in pEGFP panels are magnified in corresponding insets and identify a cell with a relatively high EGFP expression; besides a major nuclear localization due to an added nuclear localization signal (NLS), EGFP shows a diffuse cytoplasmic distribution independent of L1 ORF1p granules. Boxed areas in pPRKRA panels are magnified in corresponding insets and identify a cell with a moderate expression level of pPRKRA plasmid; exogenous 3XFLAG-PRKRA shows a cytoplasmic distribution that partially overlaps with L1 ORF1p granules (yellow arrow). Scale bars: 20 μm. **(E)** Western blot analysis of anti-ORF1p co-immunoprecipitation samples obtained from F9 cells transfected with pEGFP or pPRKRA; 3XFLAG-PRKRA co-precipitates with endogenous ORF1p. Immunoprecipitations with an isotype IgG served as negative controls. **(F)** Additional positive and negative controls for L1 retrotransposition assay. Synthetic mouse wild type (pCEPsmL1) and corresponding retrotransposition-defective control (pCEPsmL1mut) L1 elements are transfected in HeLa cells in combination with pEGFP or pPRKRA. High retrotransposition efficiency is observed using the positive control pCEPsmL1 plasmid either with pEGFP or pPRKRA; no neomycin-resistant colonies (neo^R) are generated from cells transfected with pCEPsmL1mut and pPRKRA. These data confirm that L1 retrotransposition proceeds unperturbed in the presence of PRKRA and that the obtained colonies are derived from authentic retrotransposition.

MATERIALS AND METHODS

Mice and testis samples preparation

C57BL/6 Maelstrom (*Mael*) mutant mice were previously generated [46]. C57BL/6 WT, *Mael*$^{+/-}$ and *Mael*$^{-/-}$ male mice were euthanized at ~ 3 months of age, testes were dissected and the tunica albuginea was removed in ice cold phosphate-buffered saline (PBS; 137 mM NaCl, 2.7 mM KCl, 10 mM Na_2HPO_4, 1.8 mM KH_2PO_4, pH 7.4). All procedures involving mice were performed according to ethical regulations and were approved by the IACUC of the Carnegie Institution for Science.

For electron microscopy (EM), testes were fixed and processed as described in [51]. For immunofluorescence and RNA Fluorescence In Situ Hybridization (RNA FISH), testes were fixed in freshly prepared 4% paraformaldehyde (PFA, EM grade, Electron Microscopy Sciences) in PBS for 4 hours on ice and further equilibrated in a series of sucrose solutions at increasing concentrations (10, 20 and 30% sucrose in PBS) at 4°C. Following embedding in OCT compound (Tissue-Tek), testes were sectioned into 10 µm slices on poly-L-lysine-coated slides. Slides were immediately stored at -80°C.

Antibodies

The following primary antibodies and dilutions were used: rabbit polyclonal anti-ORF1p (full length protein;[105]) diluted 1:10000 for western blot and 1:1000-1:3000 for immunofluorescence; rabbit monoclonal anti-ORF1p (Abcam, ab216324) diluted 1:1500 for western blot and 1:1000 for immunofluorescence; rabbit polyclonal anti-ribosomal protein S6/RPS6 (Novus, NB100-1595) diluted 1:1200 for western blot and 1:20 for immunofluorescence; rabbit polyclonal anti-ribosomal protein L28/RPL28 (Abcam, ab254927) diluted 1:100 for immunofluorescence; rabbit polyclonal anti-DDX6 (Bethyl, A300-460A-M) diluted 1:15 for immunofluorescence; rabbit monoclonal anti-CNOT7 (Abcam, ab195587) diluted 1:1000 for

immunofluorescence; rabbit polyclonal anti-CNOT1 (Proteintech, 14276-1-AP) diluted 1:200 for immunofluorescence; mouse monoclonal anti-DCP1A (3G4, Novus, H00055802-M06) diluted 1:100 for immunofluorescence; rabbit polyclonal anti-PRKRA (Abcam, ab31967) diluted 1:1000 for western blot; rabbit polyclonal anti-PRKRA (Epigentek, A72895) diluted 1:300 for immunofluorescence; mouse monoclonal anti-FLAG M2 (Sigma, F1804) diluted 1:1000 for western blot and 1:500 for immunofluorescence; rabbit monoclonal anti-phospho-eIF2α (Ser51) (Abcam, ab32157) diluted 1:2000 for western blot on HeLa cell extracts; rabbit monoclonal anti-phospho-eIF2α (Ser51) (Cell Signaling, 3398S) diluted 1:1000 for western blot on mouse testis extracts; rabbit polyclonal anti-eIF2α (pan) (Cell Signaling, 9722S) diluted 1:1000 for western blot; rabbit polyclonal anti-DDX4/MVH (Abcam, ab13840) diluted 1:3000 for western blot; mouse monoclonal anti-α-tubulin (Sigma, T6199) diluted 1:10000 for western blot.

The following secondary antibodies and dilutions were used: Alexa Fluor 488 donkey anti-rabbit IgG (Invitrogen, A21206), Alexa Fluor 568 donkey anti-rabbit IgG (Invitrogen, A10042), Alexa Fluor 647 donkey anti-rabbit IgG (Invitrogen, A31573) and Alexa Fluor 647 donkey anti-mouse IgG (Invitrogen, A31571) diluted 1:500 for immunofluorescence; IRDye 800CW goat anti-rabbit (LI-COR, 926-32211) and IRDye 680RD goat anti-rabbit (LI-COR, 926-68071) diluted 1:10000 for western blot.

Plasmids

The control vector pEGFP was generated by Gibson assembly [106] of the following DNA fragments: the EF-1 alpha promoter (amplified from pEF1a-mRor2WT, Addgene #2261, a gift from Roel Nusse [107]) and the EGFP-ori-AmpR fragment (amplified from pCMV_ABEmax_P2A_GFP, Addgene #112101, a gift from David Liu [108]).

The pPRKRA plasmid, expressing N-terminal 3XFLAG-tagged PRKRA (NCBI Reference Sequence: NM_011871) mouse protein, was generated by Gibson assembly of the following fragments: the EF-1 alpha promoter (from Addgene #2261), the Kozak-3XFLAG fragment (from

c3GIC9, Addgene #62191, a gift from Lukas Dow [109]), the PRKRA CDS (amplified from a *Mael*$^{-/-}$ testis cDNA sample) and the P2A-EGFP-ori-AmpR fragment (from Addgene #112101).

pTN201, pCEPsmL1 and pCEPsmL1mut plasmids have been described elsewhere [20,110] and were kindly provided by Jeffrey Han (Tulane University); pPAGFP-C1 plasmid (Addgene #11910) was a gift from Svetlana Deryusheva (Carnegie Institution for Science, Embryology).

Cell culture and DNA transfection

Human HeLa cells (kindly provided by Kamena Kostova, Carnegie Institution for Science, Embryology) and mouse F9 carcinoma cells (ATCC CRL-1720) were maintained in DMEM (Gibco, 11960051) supplemented with 10% FBS, 1X Glutamax (Gibco, 35050061) and 1X penicillin/streptomycin (Gibco, 15140122). Coating of culture surfaces with 0.1% gelatin (Sigma, G1393) was performed to improve F9 cells adhesion. Cell lines were routinely tested for Mycoplasma contamination using the Venor GeM Mycoplasma Detection Kit (Sigma, MP0025).

HeLa cells were transfected using Fugene HD reagent (Promega, E2311) at a 3:1 Transfection Reagent:DNA ratio. Cells were harvested for RNA or protein analyses 72 hours after transfection. Fugene HD only-treated cells (mock) were used as a negative control.

F9 cells were transfected using Lipofectamine STEM (Invitrogen, STEM00003). 48 hours after transfection, cells were either fixed for immunofluorescence assays or harvested for differential cytoplasmic / nuclear protein extraction or co-immunoprecipitation. Lipofectamine only-treated cells (mock) were used as a negative control in immunofluorescence assays.

Immunofluorescence

For immunofluorescence on testis sections, slides were thawed and left to dry at 42°C for 5 minutes. Sections were then rehydrated in PBS for 10 minutes at room temperature before permeabilization.

For immunofluorescence on F9 cultured cells, cells were grown on fibronectin-coated coverslips (Corning, 354088) in 6-well plates and transfected as described above. 48 hours after transfection, cells were fixed in 4% PFA in PBS for 12 minutes at room temperature and further rinsed in PBS before permeabilization.

Samples were permeabilized with 0.1% Triton X-100 in PBS for 10 minutes and blocked with 10% normal serum / 0.05% Triton X-100 in PBS for 1 hour at room temperature. Samples were then probed with the appropriate primary antibody, diluted in blocking solution with 3% normal serum, overnight at 4°C. Slides were washed once with 0.1% Triton X-100 and twice with 0.05% Triton X-100 in PBS and further incubated with the corresponding Alexa Fluor-conjugated secondary antibody diluted in blocking solution with 3% normal serum, for 1 hour and 30 minutes at room temperature. Slides were washed as above, counterstained with DAPI and mounted with ProLong Diamond Antifade Mountant (Thermo Fisher, P36961).

For immunostaining performed using two primary antibodies derived from the same species (rabbit anti-ORF1p with either rabbit anti-RPS6, rabbit anti-RPL28, rabbit anti-CNOT7, rabbit anti-DDX6, rabbit anti-CNOT1, or rabbit anti-PRKRA antibodies), samples were probed as described above using one of the two rabbit primary antibodies. Samples were then washed, briefly fixed with 4% PFA in PBS and probed again with the other rabbit primary antibody directly labeled using either the Zenon rabbit IgG labeling kits (Invitrogen, Z25302 or Z25306), or the Mix-n-Stain CF647 Antibody labeling kit (Sigma, MX647S100), according to manufacturer's instructions. To avoid cross-talk between channels, combinations of Alexa Fluor 488 with either red (568) or far red (647) Alexa Fluor fluorophores were used.

For DCP1A and ORF1p double labeling, the mouse anti-DCP1A antibody was covalently conjugated to a 488 fluorophore using the Mix-n-Stain CF488A Antibody labeling kit (Sigma, MX488AS100) and used together with the rabbit polyclonal anti-ORF1p antibody covalently conjugated to a 647 fluorophore with the Mix-n-Stain CF647 Antibody labeling kit. This strategy

eliminates the background staining generated by the use of an anti-mouse secondary antibody on mouse tissues.

Hybridization Chain Reaction (HCR) RNA FISH

HCR RNA FISH (v3.0) using split-initiator probes was performed using custom DNA probe sets, DNA HCR hairpin amplifiers, Probe Hybridization and Amplification buffers purchased from Molecular Instruments Inc. (Los Angeles, CA, USA) as described in [58] with modifications as follows. Mouse testis slides were thawed and left to dry at 42°C for 5 minutes. Sections were rehydrated in PBS and permeabilized in 0.2% Triton X-100 in PBS for 10 minutes at room temperature. Slides were then incubated with 1 ml pre-warmed (37°C) pepsinization solution (0.005% pepsin in 0.01 N HCl) for 6 minutes at room temperature to unmask the RNA. Pepsin was inactivated with 50 mM $MgCl_2$ in PBS and sections were post-fixed in 1% PFA in PBS for 10 minutes at room temperature. For RNase-treated samples, slides were further incubated with 0.2 µg/µl RNase A in PBS for 1 hour at 37°C, before proceeding with the following steps.

Slides were washed twice in 2X SSC and incubated in 50% formamide in 2X SSC for 2 hours at room temperature in a humidified chamber. The humidified chamber was then transferred to 37°C and pre-warmed for one additional hour. Slides were pre-hybridized in Probe Hybridization buffer (Molecular Instruments Inc.) for 30 minutes at 37°C, then probe solutions were added and incubated overnight at 37°C. Setx and U6 snRNA probes were used at a final concentration of 5 nM; probes directed to MMERVK10c-int and L1spa were used at a final concentration of 2.5 nM in Probe Hybridization buffer. For background estimation, probes were omitted in negative control slides. Slides were immersed in 2X SSC for 20 minutes at room temperature to remove excess probes, then washed with 0.1% Tween-20 in 0.2X SSC (multiplexed MMERVK10c-int and L1spa slides) or with 0.1% Tween-20 in 1X SSC (U6 slides, and multiplexed Setx and L1spa slides). Slides were then incubated in Amplification buffer (Molecular Instruments Inc.) for 30 minutes at room temperature before proceeding to probes

amplification using snap-cooled fluorescent HCR hairpins diluted in Amplification buffer, overnight at room temperature. Hairpins directed to Setx probes (B1 amplifier) were conjugated with Alexa 488 (B1-488); hairpins directed to U6 probes (B4 amplifier) were conjugated with Alexa 488 (B4-488); hairpins directed to MMERVK10c-int probes (B2 amplifier) were conjugated with Alexa 546 (B2-546); hairpins directed to L1spa probes (B4 amplifier) were conjugated with Alexa 647 (B4-647). Slides were immersed in 2X SSC for 15 minutes at room temperature to remove excess hairpins and then further washed with 0.1% Tween-20 in 1X SSC, four times at room temperature. Samples were counterstained with DAPI and mounted with ProLong Diamond Antifade Mountant (Thermo Fisher, P36961).

Combined immunofluorescence and HCR RNA FISH

Testis sections (Figure 1G) were first probed for L1 ORF1p (rabbit polyclonal antibody), according to the immunofluorescence protocol described previously. After the secondary antibody incubation (Alexa Fluor 488 donkey anti-rabbit IgG; Invitrogen, A21206) and the subsequent washes in PBS / Triton X-100, slides were washed twice in 2X SSC, and then transferred in 50% formamide in 2X SSC. The following FISH steps (pre-hybridization, hybridization with probes directed to L1spa, and signal amplification with Alexa 647-conjugated hairpins) were performed as described previously in the HCR RNA FISH section; all washes were performed with 0.1% Tween-20 in 1X SSC.

Microscopy and image analysis

Following immunofluorescence labeling or RNA FISH, samples were imaged using a Leica SP5 confocal laser scanning microscope or a Leica Stellaris 8 FALCON confocal microscope with LAS X software. For colocalization analyses by two-color FISH or immunofluorescence, images were acquired with settings adjusted to avoid fluorescence bleed-through and channels were scanned sequentially to obtain complete separation of the signals. Image processing was

performed using ImageJ (https://imagej.nih.gov/ij/) or with the Imaris software (Oxford Instruments).

Protein extraction

Proteins from transfected HeLa cells were extracted with RIPA buffer containing 50 mM Tris-HCl pH 8.0, 150 mM NaCl, 1% NP-40, 0.5% sodium deoxycholate, Halt protease and phosphatase inhibitors (Thermo Fisher, 78445) in water. Cells were incubated for 30 minutes on ice and lysates were centrifuged at 16,000 x *g* for 10 minutes at 4°C. Supernatants were recovered and proteins were quantified using the BCA assay kit (Thermo Scientific, 23225).

Differential cytoplasmic / nuclear protein extracts from transfected F9 cells were prepared using the NE-PER nuclear and cytoplasmic extraction reagents (Thermo Scientific, 78833), according to manufacturer's instructions.

Sucrose gradients ultracentrifugation

Testes from C57BL/6 *Mael*$^{+/-}$ and *Mael*$^{-/-}$ mice (~ 3 months of age) were dissected as previously described. For treatment with cycloheximide (CHX, Sigma-Aldrich, C4859), freshly dissected testes were transferred in ice cold PBS containing 200 µg/ml CHX and they were further homogenized in Lysis buffer containing 100 mM KCl, 20 mM Tris-HCl pH 7.5, 5 mM $MgCl_2$, 0.3% NP-40, 200 µg/ml CHX, Halt protease and phosphatase inhibitors (Thermo Fisher, 78445), RNasin Ribonuclease Inhibitor (Promega, N2515) in nuclease-free water. For treatment with EDTA, testes were homogenized in Lysis buffer containing 100 mM KCl, 20 mM Tris-HCl pH 7.5, 2 mM $MgCl_2$, 0.3% NP-40, Halt protease and phosphatase inhibitors (Thermo Fisher, 78445), RNasin Ribonuclease Inhibitor (Promega, N2515) in nuclease-free water.

Testes were homogenized using a Kontes motorized pestle and obtained lysates were incubated 20 minutes on ice. Lysates were centrifuged at 12,000 x *g* for 10 minutes at 4°C and

supernatants were recovered. For treatment with EDTA, EDTA (Invitrogen, AM9260G) was added to the supernatant at this point, at a final concentration of 10 mM.

RNA concentration was quantified using a Qubit Fluorometer (Thermo Fisher Scientific) and equal amounts of RNA (100 µg) in the same final volume (~300 µl extract) were loaded onto linear 10-50% (w/v) sucrose gradients. Gradients were centrifuged in a SW41 rotor (Beckman) at 35,000 rpm for 2 hours and 30 minutes at 4°C. For CHX gradients, sucrose solutions were prepared in 100 mM KCl, 20 mM Tris-HCl pH 7.5, 5 mM $MgCl_2$ in nuclease-free water. For EDTA gradients, sucrose was dissolved in 40 mM KCl, 25 mM Tris-HCl pH 7.5, 10 mM EDTA [57] in nuclease-free water. Sucrose gradients were fractionated using a Gradient Master station (Biocomp; 12 fractions of 1 ml each), while absorbance (254 nm) was continuously recorded to generate a UV profile of the gradient.

For treatment with RNase, samples were prepared following the EDTA treatment method described above, omitting RNasin Ribonuclease Inhibitor from the Lysis buffer. Before layering onto EDTA gradients, samples were incubated with 10 µg/ml RNase A (Invitrogen, AM2270) and 25 U/ml RNase T1 (Thermo Fisher, EN0541) for 30 minutes at room temperature with gentle mixing.

Protein precipitation

Proteins were precipitated from sucrose fractions using trichloroacetic acid (TCA; Sigma-Aldrich, T6399). Briefly, 250 µl of 50% (w/v) TCA in water were added to each 1 ml sucrose fraction, in the presence of 0.016% sodium deoxycholate as a carrier. Samples were incubated on ice for 30 minutes and then centrifuged at 16,000 x *g* for 30 minutes at 4°C. Protein pellets were washed twice with 1 ml ice-cold acetone, resuspended in 60 µl of SDS sample buffer (2% sodium dodecyl sulfate (SDS), 50 mM Tris-HCl pH 6.8, 10% glycerol, 100 mM dithiothreitol (DTT), 0.003% bromophenol blue in water) and resolved on 12% SDS-polyacrylamide gels.

Western blot

Proteins were resolved on SDS-polyacrylamide gels and transferred onto PVDF Immobilon-FL membranes (Millipore, IPFL00010). Membranes were blocked with Intercept blocking buffer in PBS (LI-COR, 927-70001) or with 3% Bovine Serum Albumin (BSA) in Tris-buffered saline (TBS; 150 mM NaCl, 20 mM Tris-HCl, pH 7.6) for phospho-eIF2α detection, for one hour at room temperature. Membranes were probed with primary antibodies diluted in Intercept blocking buffer containing 0.1% Tween-20 or with anti-phospo-eIF2α antibodies diluted in 1% BSA in TBS, overnight at 4°C. Membranes were washed three times with PBS or TBS containing 0.1% Tween-20 and further incubated with IRDye-conjugated secondary antibodies (LI-COR) diluted in the same buffer used for the corresponding primary antibody, for one hour at room temperature. Membranes were washed three times and signals were detected with the Odyssey CLx imaging system (LI-COR).

Signals were quantified with Image Studio software v5.2.5 (LI-COR). The stripping buffer used for blot #1 in Figure 6E is NewBlot PVDF Stripping buffer (LI-COR, 928-40032), according to manufacturer's guidelines.

RNA extraction

RNA from 500 µl of each sucrose fraction or from a fraction (5%) of the gradient input was extracted by adding 500 µl of TRIzol reagent (Invitrogen) followed by 200 µl of chloroform. Samples were incubated at room temperature for 10 minutes with gentle agitation and then centrifuged at 12,000 x *g* for 15 minutes at 4°C. Supernatants were collected and RNA was precipitated with 1 volume of isopropanol and 1 µl of GlycoBlue (Invitrogen, AM9515). RNA was recovered by centrifugation at 12,000 x *g* for 30 minutes at 4°C. RNA pellets were washed with ice-cold 75% ethanol in nuclease-free water and further resuspended in 11 µl of nuclease-free water. 5 µl were used for DNase treatment with TURBO DNase (Invitrogen, AM2238) in 10 µl final volume and further processed for cDNA synthesis.

RNA from transfected HeLa cells was extracted with 500 µl of TRIzol reagent (Invitrogen) and further purified with Direct-zol RNA Miniprep kit (Zymo research, R2050), according to manufacturer's protocol. 2 µg per sample were used for DNase treatment with TURBO DNase (Invitrogen) and further processed for cDNA synthesis.

cDNA synthesis and qRT-PCR

DNase-treated RNA was divided in 2 samples of equal volume (+RT and -RT) and processed for cDNA synthesis using an oligo$(dT)_{20}$ and the SuperScript III first-strand synthesis system (Invitrogen, 18080051), according to manufacturer's instructions. The reverse transcriptase was omitted in -RT samples.

cDNA samples obtained from sucrose fractions were diluted 1:35 in nuclease-free water, while samples obtained from gradient inputs were diluted 1:100; cDNA samples from human HeLa cells were diluted 1:80 in nuclease-free water. 4 µl of diluted cDNAs were added to each PCR reaction containing the SsoAdvanced Universal SYBR Green Supermix (Bio-Rad, 1725271) and primers at a final concentration of 300 nM each, in a final volume of 10 µl. The following primer couples were used: ORF1-For: ATG GCG AAA GGT AAA CGG AG, ORF1-Rev: AGT CCT TCT TGA TGT CCT CT (for mouse L1 ORF1); mActb-For: CGG TTC CGA TGC CCT GAG GCT CTT, mActb-Rev: CGT CAC ACT TCA TGA TGG AAT TGA (for mouse beta-actin); hGAPDH-For: AAT CCC ATC ACC ATC TTC CAG, hGAPDH-Rev: AAA TGA GCC CCA GCC TTC (for human GAPDH).

Mean (n=3) Ct (threshold cycle) values were used to quantify mRNA levels. The distribution of ORF1 and beta-actin mRNAs in sucrose gradients was determined using the ΔCt method. The Ct value of the gradient input was set as the reference and obtained values were further converted into percentages. Relative quantities of mouse ORF1 in transfected HeLa cells were analyzed using the ΔΔCt method, with human GAPDH as the reference gene.

Co-immunoprecipitation

Proteins from testes and from transfected F9 cells were extracted using the same Lysis buffer described previously for sucrose gradients ultracentrifugation (treatment with EDTA). Protein concentrations were determined with BCA assay (Thermo Scientific, 23225). For RNase treatment before co-immunoprecipitation, RNA concentration in extracts was determined using a Qubit Fluorometer (Thermo Fisher Scientific) and samples containing approximately 50 µg RNA were incubated with 10 µg/ml RNase A (Invitrogen, AM2270), 25 U/ml RNase T1 (Thermo Fisher, EN0541) and 50 U/ml RNase I (Lucigen, N6901K) for 30 minutes at room temperature with gentle mixing. In these cases, RNasin Ribonuclease Inhibitor was omitted from the Lysis buffer.

For co-immunoprecipitation followed by RNA-seq (Figure 3A-D), pools of sucrose fractions 5, 6, 7 and 8 - obtained from *Mael*$^{-/-}$ testicular extracts (TOTAL) fractionated in the presence of EDTA - were used as input (INPUT) for either anti-ORF1p immunoprecipitations (IP) or incubations with beads only (BO).

Rabbit monoclonal anti-ORF1p antibody (Abcam, ab216324) or rabbit IgG isotype (Abcam, ab172730) were coupled to Dynabeads M-270 Epoxy, using the Dynabeads Antibody Coupling kit (Invitrogen, 14311D) at a ratio of 10 µg ligand per mg of beads. For BO samples, the ligand was substituted with an equivalent volume of buffer C1 of the kit. 1.5 - 2 mg of beads were added to 1.5 - 2 mg of proteins or to pools of 5-8 fractions and incubated for 2 hours and 30 minutes at 4°C. Beads were washed four times in 100 mM KCl, 20 mM Tris-HCl pH 8.0, 0.3% NP-40, Halt protease and phosphatase inhibitors in nuclease-free water, for 5 minutes at 4°C with rotation. For samples washed at a higher stringency, beads were washed twice as above and twice in the same buffer with a higher concentration of KCl (300 mM). After the last wash, samples were transferred to clean tubes. For western blot and silver staining in polyacrylamide gels (SilverQuest staining kit; Invitrogen, 45-1001), precipitated proteins were eluted with 0.2 M Glycine pH 2.6. For RNA-seq, RNA was eluted by adding TRIzol reagent to Dynabeads and extracted as previously described.

Mass spectrometry and data analysis

For LC/MS/MS analyses, elution of immunoprecipitated proteins was performed at Poochon Scientific (Frederick, MD, USA) as follows. Dynabeads were dissolved in 2% SDS, 25 mM NH_4HCO_3, 10 mM DTT in water. Samples were denatured at 95°C and then processed for in-solution trypsin digestion. The digested peptide mixture was then concentrated and desalted. Desalted peptides were reconstituted in 20 µl of 0.1% formic acid, of which 16 µl were analyzed by LC/MS/MS.

The LC/MS/MS analysis of samples was carried out using a Thermo Scientific Q-Exactive Hybrid Quadrupole-Orbitrap Mass Spectrometer and a Thermo Dionex UltiMate 3000 RSLCnano System. Peptide mixtures from each sample were loaded onto a peptide trap cartridge at a flow rate of 5 µL/min. The trapped peptides were eluted onto a reversed-phase PicoFrit column (New Objective, MA) using a linear gradient of acetonitrile (3-36%) in 0.1% formic acid. Eluted peptides from the PicoFrit column were ionized and sprayed into the mass spectrometer, using a Nanospray Flex Ion Source ES071 (Thermo) under the following settings: spray voltage 1.8 kV; capillary temperature 250°C. Other settings were empirically determined.

The raw data files acquired from each sample were searched against mouse protein sequences database using the Proteome Discoverer 1.4 software (Thermo Scientific) based on the SEQUEST algorithm. The Carbamidomethylation (+57.021 Da) of cysteines was set as a fixed modification, whereas Oxidation Met and Deamidation Q/N-deamidated (+0.98402 Da) were set as dynamic modifications. The minimum peptide length was specified to be 5 amino acids. The precursor mass tolerance was set to 15 ppm, whereas fragment mass tolerance was set to 0.05 Da. The maximum false peptide discovery rate was specified as 0.01. The resulting Proteome Discoverer Report contains all assembled proteins, with Peptide Spectrum Match (PSM) counts.

PSM counts were used to determine the abundance of the corresponding protein in each eluate. For background subtraction based on PSM counts in negative controls (BO or IgG

isotype), proteins showing the same or higher counts in negative controls than corresponding IP samples were excluded from subsequent analyses. Furthermore, proteins with PSM counts ≥ 10 in negative controls and with a difference < 3 between IP samples and negative controls were also excluded. For the evaluation of behavior at higher stringency conditions, proteins decreased more than three times or completely lost upon higher stringency washes (300 mM KCl) were filtered out. Only proteins common to all replicates were considered for further analyses. This strategy returned n=80 high confidence ORF1p interactors.

The relative abundance of the identified proteins in each eluate was then calculated by adjusting the PSM counts to molecular weights (MW in kDa) [111]. To allow a sample-to-sample comparison of abundances, the obtained PSM / MW ratios were further normalized to the ratio obtained for the bait (L1 ORF1p). Physical and functional interactions were retrieved using the STRING database v11.5 (https://string-db.org/; [67]).

RNA-seq analysis

A total of 200 ng RNA (for TOTAL and INPUT samples), 20-40 ng RNA (for IP samples) and the RNA yield in the same volume of corresponding IP samples (for BO samples) were treated with TURBO DNase (Invitrogen, AM1907) in 10 µl final volume. Libraries were generated using the TruSeq Stranded Total RNA kit (Illumina) with Ribo-Zero rRNA depletion. 75 bp single-end reads were sequenced on an Illumina NextSeq 500 system.

For genomic repeats analysis, reads were mapped to mouse mm10 reference genome using STAR v2.6.0c [112], option --outFilterMultimapNmax 100. The obtained .bam file was used as input for Telescope v1.0.3 [113] to reassign ambiguously mapped reads. The updated counts were collapsed to single repeat subfamilies using a custom Perl script and normalized using EBSeq v1.26.0 [114] in R.

For coding genes analysis, reads were mapped to mouse mm10 using STAR v2.6.0c. Read counts were normalized using DESeq2 v1.24.0 [115] in R. Genes were considered

significatively enriched with a log2 Fold Change > 1 and a padj < 0.05. Transcript lengths (including UTRs and CDS) for n=2081 L1 ORF1p-bound mRNAs were retrieved from Ensembl using the biomaRt package in R. The max transcript length value was used for the correlation analysis in Figure 3D. Gene ontology analysis was performed using DAVID Bioinformatics Resources v6.8.

Ribosome profiling

Lysates were generated from postnatal day 16 (P16) C57BL/6 *Mael*$^{+/-}$ and *Mael*$^{-/-}$ testes. Testes were homogenized in Lysis buffer [116] supplemented with Halt protease and phosphatase inhibitors (Thermo Fisher, 78445) and Murine RNase inhibitor (New England Biolabs, M0314S), using a Kontes motorized pestle. Lysates were clarified by centrifugation at 12,000 x *g* for 10 minutes at 4°C. Supernatants were recovered and the RNA concentration was determined using a Qubit Fluorometer (Thermo Fisher Scientific). To generate monosomes, 20 µg of RNA per sample were incubated with 5U MNase (Takara Bio, 2910A) supplemented with 5 mM $CaCl_2$ in 200 µl final volume, for 1 hour at room temperature with gentle agitation. Reactions were quenched with 6.25 mM EGTA. Digested extracts were then loaded on 1 M sucrose cushions [116] and centrifuged at 70,000 rpm for 2 hours at 4°C in a TLA100.4 rotor (Beckman). Ribosome pellets were resuspended in 300 µl of TRIzol reagent (Invitrogen). At this point, aliquots of testicular extracts containing 2.5 µg of total RNA were also resuspended in 300 µl of TRIzol to recover RNA for the corresponding RNA-seq analysis. All samples were purified using the Direct-zol RNA Miniprep kit (Zymo Research, R2050), including the in-column DNase I treatment.

Total RNA samples were further processed to generate libraries using the TruSeq Stranded Total RNA kit (Illumina) with Ribo-Zero rRNA depletion. RNA purified from ribosome pellets was instead processed for ribosome footprints purification (28-34 nt) and libraries generation, as described in [116], with the following modifications. Our 5' adenylated linker sequence is: /5rApp/NNN NNA TCG AGA TCG GAA GAG CAC ACG TCT GAA CTC/3ddC/ [117]. Footprints

were reverse transcribed with the SuperScript III first-strand synthesis system (Invitrogen, 18080051) for 40 minutes at 55°C, using the following reverse transcription primer: /5Phos/AGA TCG GAA GAG CGT CGT GTA GGG AAA GAG/iSp18/CTG GAG TTC AGA CGT GTG [117].

75 bp single-end reads were sequenced on an Illumina NextSeq 500 system. Ribo-seq reads were preprocessed with FASTX-Toolkit v0.0.14 (http://hannonlab.cshl.edu/fastx_toolkit/) to clip the linker sequence (ATC GAG ATC GGA AGA GCA CAC GTC TGA ACT C) and trim the UMI (5Ns) from the 3' end. Clipped Ribo-seq reads were aligned to mouse ribosomal DNA (Genbank: BK000964.1) using Bowtie v1.2.2 [118] to collect unaligned reads. Non-rRNA Ribo-seq reads and corresponding RNA-seq reads were then mapped to mouse mm10 reference genome using STAR v2.6.0c [112] and counted using featureCounts (Subread package v1.6.4; [119]). Reads were counted on the entire mRNA length for RNA-seq datasets, or only on CDS for Ribo-seq datasets to get footprints generated from actively translating ribosomes. Counts were normalized and translation efficiency was calculated using DESeq2 v1.24.0 [115] in R.

Poly(A) tail length assay

Total RNA was extracted from P16 testicular extracts prepared as described above for ribosome profiling, using the Direct-zol RNA Miniprep kit (Zymo Research, R2050), including the in-column DNase I treatment. 500 ng of RNA were subjected to poly(U) tailing using poly(U) Polymerase (New England Biolabs, M0337S) in 1X NEBuffer 2 for 30 minutes at 37°C. 160 ng of polyuridylated RNA were processed for cDNA synthesis using an RT adapter (GCG AGC ACA GAA TTA ATA CGA CTC ACT ATA GGA AAA AAA AAA AAT T) and the SuperScript III first-strand synthesis system (Invitrogen, 18080051), according to manufacturer's instructions. The obtained cDNA samples were PCR amplified using a forward primer mapping to the 3'UTR of the gene of interest and a reverse primer annealing to the RT adapter. Primers were used at a final concentration of 800 nM each and have the following sequences: Sycp1-3'UTR-For: GAG AGC CAA ACT TTA CCA AGG A; Setx-3'UTR-For: ACC TGT CTT ACT TTG CTT CTC TC; Adapter-

Rev: GCG AGC ACA GAA TTA ATA CGA CT. PCR amplifications were performed using GoTaq DNA Polymerase (Promega, M3001), according to manufacturer's instructions; samples were visualized on 1.5% agarose gels.

Retrotransposition assay

L1 retrotransposition assay was performed as previously described [34] with minor modifications. Briefly, HeLa cells were seeded in 6-well plates in supplemented DMEM culture medium. Seeding densities were optimized to obtain quantifiable G418-resistant colonies in every condition. For assays employing native mouse wild type L1 (pTN201) and for negative controls (synthetic mouse mutant L1 (pCEPsmL1mut) and mock treatment), 2 x 10^4 cells were plated in each well. For assays employing synthetic mouse wild type L1 (pCEPsmL1), 800 cells were plated per well. For the control reporter plasmid (pPAGFP-C1), 2 x 10^3 cells were plated per well.

The next day cells were transfected with 500 ng of L1 plasmids plus equimolar amounts of either pEGFP or pPRKRA constructs, diluted in 77 µl of Opti-MEM (Gibco, 31985062), using 2 µl of Fugene HD transfection reagent (Promega). The control reporter plasmid was transfected in parallel in equimolar amounts with pEGFP or pPRKRA. Transfection was blocked after 7 hours by replacing the medium with fresh DMEM.

48 hours post-transfection, live cells were imaged at an Eclipse Ti2 inverted microscope (Nikon) to determine the transfection efficiency for every experimental condition. Both brightfield and GFP images were acquired for the same cells, allowing a direct estimation of the number of $EGFP^+$ over the total number of cells. 72 hours post-transfection, G418 selection (400 µg/ml; Gibco, 10131035) was started. Medium was replaced every day until 14 days post-transfection. G418-resistant colonies were then fixed with 4% PFA in PBS for 1 hour and 30 minutes at room temperature and stained with 0.1% crystal violet (Sigma, V5265) in water.

Images of whole wells containing stained colonies were acquired on a Zeiss AxioZoom.V16 macroscope with Zen software (Zeiss). Using the Integrated Morphometry

Analysis module of MetaMorph software (Molecular Devices), the images were segmented to separate colonies from isolated cells and irregular non-colony clusters. Colonies were identified on the basis of size, shape and uniformity of staining (minimum diameter 194.5 μm, circularity ≥ 0.45, gray level texture difference moment ≤ 2.75 [120]), and then counted. Over- and under-segmented colony counts were corrected by manual proofreading. Colony counts were obtained from three technical replicates per experimental condition. Mean colony counts were calculated and further adjusted for transfection efficiency to obtain the adjusted retrotransposition mean. The adjusted retrotransposition mean obtained for native mouse L1 (pTN201) was then divided by the value obtained for the control reporter plasmid (pPAGFP-C1) to calculate the corrected retrotransposition mean. The corrected retrotransposition mean was further converted to corrected retrotransposition efficiency to estimate the retrotransposition efficiency of pTN201 in the presence of pPRKRA, in comparison to pEGFP control (set as 100%).

Supplemental Tables

Table S1. mRNAs bound by L1 ORF1p in *Mael*$^{-/-}$ testes (n=2081) with their corresponding enrichment in IP samples (log2FoldChange and p-adjusted values); related to Figure 3B, 3C and 3D.

Table S2. Gene Ontology analysis (Biological Process) of the set of mRNAs strongly enriched in anti-ORF1p IP samples (n=1347); related to Figures 3B and S3B.

Table S3. Mass spectrometry analysis of L1 ORF1p interactors: raw data and proteins retained after background subtraction from two independent experiments (E1, E2); related to Figure 4.

Table S4. High confidence L1 ORF1p interactors (n=80); related to Figure 4.

Table S5. Comparison of L1 ORF1p interactors identified in this study (mouse proteins) with previously published human datasets; related to Figure 4.

References

1. Wells, J.N., and Feschotte, C. (2020). A Field Guide to Eukaryotic Transposable Elements. Annu Rev Genet *54*, 539-561. 10.1146/annurev-genet-040620-022145.

2. Kojima, K.K. (2020). Structural and sequence diversity of eukaryotic transposable elements. Genes Genet Syst *94*, 233-252. 10.1266/ggs.18-00024.

3. Kazazian, H.H., Jr. (2004). Mobile elements: drivers of genome evolution. Science (New York, N.Y.) *303*, 1626-1632. 10.1126/science.1089670.

4. Almojil, D., Bourgeois, Y., Falis, M., Hariyani, I., Wilcox, J., and Boissinot, S. (2021). The Structural, Functional and Evolutionary Impact of Transposable Elements in Eukaryotes. Genes (Basel) *12*. 10.3390/genes12060918.

5. Senft, A.D., and Macfarlan, T.S. (2021). Transposable elements shape the evolution of mammalian development. Nat Rev Genet *22*, 691-711. 10.1038/s41576-021-00385-1.

6. Platt, R.N., 2nd, Vandewege, M.W., and Ray, D.A. (2018). Mammalian transposable elements and their impacts on genome evolution. Chromosome Res *26*, 25-43. 10.1007/s10577-017-9570-z.

7. Hancks, D.C., and Kazazian, H.H., Jr. (2016). Roles for retrotransposon insertions in human disease. Mob DNA *7*, 9. 10.1186/s13100-016-0065-9.

8. Richardson, S.R., Doucet, A.J., Kopera, H.C., Moldovan, J.B., Garcia-Perez, J.L., and Moran, J.V. (2015). The Influence of LINE-1 and SINE Retrotransposons on Mammalian

Genomes. Microbiology spectrum *3*, Mdna3-0061-2014. 10.1128/microbiolspec.MDNA3-0061-2014.

9. Zemach, A., and Zilberman, D. (2010). Evolution of eukaryotic DNA methylation and the pursuit of safer sex. Curr Biol *20*, R780-785. 10.1016/j.cub.2010.07.007.

10. Deniz, O., Frost, J.M., and Branco, M.R. (2019). Regulation of transposable elements by DNA modifications. Nat Rev Genet *20*, 417-431. 10.1038/s41576-019-0106-6.

11. Molaro, A., and Malik, H.S. (2016). Hide and seek: how chromatin-based pathways silence retroelements in the mammalian germline. Curr Opin Genet Dev *37*, 51-58. 10.1016/j.gde.2015.12.001.

12. Castaneda, J., Genzor, P., and Bortvin, A. (2011). piRNAs, transposon silencing, and germline genome integrity. Mutat Res *714*, 95-104. 10.1016/j.mrfmmm.2011.05.002.

13. Iwasaki, Y.W., Siomi, M.C., and Siomi, H. (2015). PIWI-Interacting RNA: Its Biogenesis and Functions. Annu Rev Biochem *84*, 405-433. 10.1146/annurev-biochem-060614-034258.

14. Goodier, J.L., and Kazazian, H.H., Jr. (2008). Retrotransposons revisited: the restraint and rehabilitation of parasites. Cell *135*, 23-35. 10.1016/j.cell.2008.09.022.

15. Bruno, M., Mahgoub, M., and Macfarlan, T.S. (2019). The Arms Race Between KRAB-Zinc Finger Proteins and Endogenous Retroelements and Its Impact on Mammals. Annu Rev Genet *53*, 393-416. 10.1146/annurev-genet-112618-043717.

16. Moldovan, J.B., and Moran, J.V. (2015). The Zinc-Finger Antiviral Protein ZAP Inhibits LINE and Alu Retrotransposition. PLoS Genet *11*, e1005121. 10.1371/journal.pgen.1005121.

17. Goodier, J.L., Pereira, G.C., Cheung, L.E., Rose, R.J., and Kazazian, H.H., Jr. (2015). The Broad-Spectrum Antiviral Protein ZAP Restricts Human Retrotransposition. PLoS Genet *11*, e1005252. 10.1371/journal.pgen.1005252.

18. Gutierrez, J., Platt, R., Opazo, J.C., Ray, D.A., Hoffmann, F., and Vandewege, M. (2021). Evolutionary history of the vertebrate Piwi gene family. PeerJ *9*, e12451. 10.7717/peerj.12451.

19. Maksakova, I.A., Romanish, M.T., Gagnier, L., Dunn, C.A., van de Lagemaat, L.N., and Mager, D.L. (2006). Retroviral elements and their hosts: insertional mutagenesis in the mouse germ line. PLoS Genet *2*, e2. 10.1371/journal.pgen.0020002.

20. Naas, T.P., DeBerardinis, R.J., Moran, J.V., Ostertag, E.M., Kingsmore, S.F., Seldin, M.F., Hayashizaki, Y., Martin, S.L., and Kazazian, H.H. (1998). An actively retrotransposing, novel subfamily of mouse L1 elements. EMBO J *17*, 590-597. 10.1093/emboj/17.2.590.

21. Sassaman, D.M., Dombroski, B.A., Moran, J.V., Kimberland, M.L., Naas, T.P., DeBerardinis, R.J., Gabriel, A., Swergold, G.D., and Kazazian, H.H., Jr. (1997). Many human L1 elements are capable of retrotransposition. Nat Genet *16*, 37-43. 10.1038/ng0597-37.

22. Beck, C.R., Collier, P., Macfarlane, C., Malig, M., Kidd, J.M., Eichler, E.E., Badge, R.M., and Moran, J.V. (2010). LINE-1 retrotransposition activity in human genomes. Cell *141*, 1159-1170. 10.1016/j.cell.2010.05.021.

23. Cosby, R.L., Chang, N.C., and Feschotte, C. (2019). Host-transposon interactions: conflict, cooperation, and cooption. Genes Dev *33*, 1098-1116. 10.1101/gad.327312.119.

24. Jacobs, F.M., Greenberg, D., Nguyen, N., Haeussler, M., Ewing, A.D., Katzman, S., Paten, B., Salama, S.R., and Haussler, D. (2014). An evolutionary arms race between KRAB zinc-finger genes ZNF91/93 and SVA/L1 retrotransposons. Nature *516*, 242-245. 10.1038/nature13760.

25. Ostertag, E.M., and Kazazian, H.H., Jr. (2001). Biology of mammalian L1 retrotransposons. Annu Rev Genet *35*, 501-538. 10.1146/annurev.genet.35.102401.091032.

26. Hoyt, S.J., Storer, J.M., Hartley, G.A., Grady, P.G.S., Gershman, A., de Lima, L.G., Limouse, C., Halabian, R., Wojenski, L., Rodriguez, M., et al. (2022). From telomere to telomere: The transcriptional and epigenetic state of human repeat elements. Science (New York, N.Y.) *376*, eabk3112. 10.1126/science.abk3112.

27. Lindblad-Toh, K., Wade, C.M., Mikkelsen, T.S., Karlsson, E.K., Jaffe, D.B., Kamal, M., Clamp, M., Chang, J.L., Kulbokas, E.J., 3rd, Zody, M.C., et al. (2005). Genome sequence, comparative analysis and haplotype structure of the domestic dog. Nature *438*, 803-819. 10.1038/nature04338.

28. Church, D.M., Goodstadt, L., Hillier, L.W., Zody, M.C., Goldstein, S., She, X., Bult, C.J., Agarwala, R., Cherry, J.L., DiCuccio, M., et al. (2009). Lineage-specific biology revealed by a finished genome assembly of the mouse. PLoS Biol *7*, e1000112. 10.1371/journal.pbio.1000112.

29. Feng, Q., Moran, J.V., Kazazian, H.H., Jr., and Boeke, J.D. (1996). Human L1 retrotransposon encodes a conserved endonuclease required for retrotransposition. Cell *87*, 905-916.

30. Kulpa, D.A., and Moran, J.V. (2006). Cis-preferential LINE-1 reverse transcriptase activity in ribonucleoprotein particles. Nature structural & molecular biology *13*, 655-660. 10.1038/nsmb1107.

31. Wei, W., Gilbert, N., Ooi, S.L., Lawler, J.F., Ostertag, E.M., Kazazian, H.H., Boeke, J.D., and Moran, J.V. (2001). Human L1 retrotransposition: cis preference versus trans complementation. Mol Cell Biol *21*, 1429-1439. 10.1128/mcb.21.4.1429-1439.2001.

32. Cost, G.J., Feng, Q., Jacquier, A., and Boeke, J.D. (2002). Human L1 element target-primed reverse transcription in vitro. EMBO J *21*, 5899-5910. 10.1093/emboj/cdf592.

33. Luan, D.D., and Eickbush, T.H. (1995). RNA template requirements for target DNA-primed reverse transcription by the R2 retrotransposable element. Mol Cell Biol *15*, 3882-3891. 10.1128/MCB.15.7.3882.

34. Kopera, H.C., Larson, P.A., Moldovan, J.B., Richardson, S.R., Liu, Y., and Moran, J.V. (2016). LINE-1 Cultured Cell Retrotransposition Assay. Methods Mol Biol *1400*, 139-156. 10.1007/978-1-4939-3372-3_10.

35. Moran, J.V., Holmes, S.E., Naas, T.P., DeBerardinis, R.J., Boeke, J.D., and Kazazian, H.H., Jr. (1996). High frequency retrotransposition in cultured mammalian cells. Cell *87*, 917-927. 10.1016/s0092-8674(00)81998-4.

36. Ostertag, E.M., Prak, E.T., DeBerardinis, R.J., Moran, J.V., and Kazazian, H.H., Jr. (2000). Determination of L1 retrotransposition kinetics in cultured cells. Nucleic Acids Res *28*, 1418-1423. 10.1093/nar/28.6.1418.

37. Goodier, J.L., Cheung, L.E., and Kazazian, H.H., Jr. (2013). Mapping the LINE1 ORF1 protein interactome reveals associated inhibitors of human retrotransposition. Nucleic Acids Res *41*, 7401-7419. 10.1093/nar/gkt512.

38. Doucet, A.J., Hulme, A.E., Sahinovic, E., Kulpa, D.A., Moldovan, J.B., Kopera, H.C., Athanikar, J.N., Hasnaoui, M., Bucheton, A., Moran, J.V., and Gilbert, N. (2010). Characterization of LINE-1 ribonucleoprotein particles. PLoS Genet *6*. 10.1371/journal.pgen.1001150.

39. Taylor, M.S., Altukhov, I., Molloy, K.R., Mita, P., Jiang, H., Adney, E.M., Wudzinska, A., Badri, S., Ischenko, D., Eng, G., et al. (2018). Dissection of affinity captured LINE-1 macromolecular complexes. Elife *7*. 10.7554/eLife.30094.

40. Taylor, M.S., LaCava, J., Mita, P., Molloy, K.R., Huang, C.R., Li, D., Adney, E.M., Jiang, H., Burns, K.H., Chait, B.T., et al. (2013). Affinity proteomics reveals human host factors implicated in discrete stages of LINE-1 retrotransposition. Cell *155*, 1034-1048. 10.1016/j.cell.2013.10.021.

41. Mita, P., Wudzinska, A., Sun, X., Andrade, J., Nayak, S., Kahler, D.J., Badri, S., LaCava, J., Ueberheide, B., Yun, C.Y., et al. (2018). LINE-1 protein localization and functional dynamics during the cell cycle. Elife *7*. 10.7554/eLife.30058.

42. Goodier, J.L., Zhang, L., Vetter, M.R., and Kazazian, H.H., Jr. (2007). LINE-1 ORF1 protein localizes in stress granules with other RNA-binding proteins, including components of RNA interference RNA-induced silencing complex. Mol Cell Biol *27*, 6469-6483. 10.1128/MCB.00332-07.

43. Ivanov, P., Kedersha, N., and Anderson, P. (2019). Stress Granules and Processing Bodies in Translational Control. Cold Spring Harb Perspect Biol *11*. 10.1101/cshperspect.a032813.

44. Khong, A., Matheny, T., Jain, S., Mitchell, S.F., Wheeler, J.R., and Parker, R. (2017). The Stress Granule Transcriptome Reveals Principles of mRNA Accumulation in Stress Granules. Mol Cell *68*, 808-820 e805. 10.1016/j.molcel.2017.10.015.

45. Genzor, P., and Bortvin, A. (2015). A unique HMG-box domain of mouse Maelstrom binds structured RNA but not double stranded DNA. PLoS One *10*, e0120268. 10.1371/journal.pone.0120268.

46. Soper, S.F., van der Heijden, G.W., Hardiman, T.C., Goodheart, M., Martin, S.L., de Boer, P., and Bortvin, A. (2008). Mouse maelstrom, a component of nuage, is essential for spermatogenesis and transposon repression in meiosis. Dev Cell *15*, 285-297. 10.1016/j.devcel.2008.05.015.

47. Chang, T.H., Mattei, E., Gainetdinov, I., Colpan, C., Weng, Z., and Zamore, P.D. (2019). Maelstrom Represses Canonical Polymerase II Transcription within Bi-directional piRNA Clusters in Drosophila melanogaster. Mol Cell *73*, 291-303 e296. 10.1016/j.molcel.2018.10.038.

48. Matsumoto, N., Sato, K., Nishimasu, H., Namba, Y., Miyakubi, K., Dohmae, N., Ishitani, R., Siomi, H., Siomi, M.C., and Nureki, O. (2015). Crystal Structure and Activity of the Endoribonuclease Domain of the piRNA Pathway Factor Maelstrom. Cell Rep *11*, 366-375. 10.1016/j.celrep.2015.03.030.

49. Sato, K., and Siomi, M.C. (2015). Functional and structural insights into the piRNA factor Maelstrom. FEBS Lett *589*, 1688-1693. 10.1016/j.febslet.2015.03.023.

50. Aravin, A.A., van der Heijden, G.W., Castaneda, J., Vagin, V.V., Hannon, G.J., and Bortvin, A. (2009). Cytoplasmic compartmentalization of the fetal piRNA pathway in mice. PLoS Genet *5*, e1000764. 10.1371/journal.pgen.1000764.

51. Castaneda, J., Genzor, P., van der Heijden, G.W., Sarkeshik, A., Yates, J.R., 3rd, Ingolia, N.T., and Bortvin, A. (2014). Reduced pachytene piRNAs and translation underlie spermiogenic arrest in Maelstrom mutant mice. EMBO J *33*, 1999-2019. 10.15252/embj.201386855.

52. Gaysinskaya, V., Miller, B.F., De Luca, C., van der Heijden, G.W., Hansen, K.D., and Bortvin, A. (2018). Transient reduction of DNA methylation at the onset of meiosis in male mice. Epigenetics Chromatin *11*, 15. 10.1186/s13072-018-0186-0.

53. Malki, S., van der Heijden, G.W., O'Donnell, K.A., Martin, S.L., and Bortvin, A. (2014). A role for retrotransposon LINE-1 in fetal oocyte attrition in mice. Dev Cell *29*, 521-533. 10.1016/j.devcel.2014.04.027.

54. Tharp, M.E., Malki, S., and Bortvin, A. (2020). Maximizing the ovarian reserve in mice by evading LINE-1 genotoxicity. Nat Commun *11*, 330. 10.1038/s41467-019-14055-8.

55. Ayache, J., Benard, M., Ernoult-Lange, M., Minshall, N., Standart, N., Kress, M., and Weil, D. (2015). P-body assembly requires DDX6 repression complexes rather than decay or Ataxin2/2L complexes. Mol Biol Cell *26*, 2579-2595. 10.1091/mbc.E15-03-0136.

56. Gilks, N., Kedersha, N., Ayodele, M., Shen, L., Stoecklin, G., Dember, L.M., and Anderson, P. (2004). Stress granule assembly is mediated by prion-like aggregation of TIA-1. Mol Biol Cell *15*, 5383-5398. 10.1091/mbc.e04-08-0715.

57. Martin, S.L. (1991). Ribonucleoprotein particles with LINE-1 RNA in mouse embryonal carcinoma cells. Mol Cell Biol *11*, 4804-4807.

58. Choi, H.M.T., Schwarzkopf, M., Fornace, M.E., Acharya, A., Artavanis, G., Stegmaier, J., Cunha, A., and Pierce, N.A. (2018). Third-generation in situ hybridization chain reaction: multiplexed, quantitative, sensitive, versatile, robust. Development *145*. 10.1242/dev.165753.

59. Riggs, C.L., Kedersha, N., Ivanov, P., and Anderson, P. (2020). Mammalian stress granules and P bodies at a glance. J Cell Sci *133*. 10.1242/jcs.242487.

60. Kulpa, D.A., and Moran, J.V. (2005). Ribonucleoprotein particle formation is necessary but not sufficient for LINE-1 retrotransposition. Human molecular genetics *14*, 3237-3248. 10.1093/hmg/ddi354.

61. Hohjoh, H., and Singer, M.F. (1996). Cytoplasmic ribonucleoprotein complexes containing human LINE-1 protein and RNA. Embo j *15*, 630-639.

62. Mandal, P.K., Ewing, A.D., Hancks, D.C., and Kazazian, H.H., Jr. (2013). Enrichment of processed pseudogene transcripts in L1-ribonucleoprotein particles. Human molecular genetics *22*, 3730-3748. 10.1093/hmg/ddt225.

63. Briggs, E.M., McKerrow, W., Mita, P., Boeke, J.D., Logan, S.K., and Fenyo, D. (2021). RIP-seq reveals LINE-1 ORF1p association with p-body enriched mRNAs. Mob DNA *12*, 5. 10.1186/s13100-021-00233-3.

64. Dewannieux, M., and Heidmann, T. (2005). LINEs, SINEs and processed pseudogenes: parasitic strategies for genome modeling. Cytogenetic and genome research *110*, 35-48. 10.1159/000084936.

65. Dewannieux, M., Esnault, C., and Heidmann, T. (2003). LINE-mediated retrotransposition of marked Alu sequences. Nat Genet *35*, 41-48. 10.1038/ng1223.

66. Kershaw, C.J., Nelson, M.G., Lui, J., Bates, C.P., Jennings, M.D., Hubbard, S.J., Ashe, M.P., and Grant, C.M. (2021). Integrated multi-omics reveals common properties underlying stress granule and P-body formation. RNA Biol *18*, 655-673. 10.1080/15476286.2021.1976986.

67. Szklarczyk, D., Gable, A.L., Nastou, K.C., Lyon, D., Kirsch, R., Pyysalo, S., Doncheva, N.T., Legeay, M., Fang, T., Bork, P., et al. (2021). The STRING database in 2021: customizable protein-protein networks, and functional characterization of user-uploaded gene/measurement sets. Nucleic Acids Res *49*, D605-D612. 10.1093/nar/gkaa1074.

68. Taha, M.S., Haghighi, F., Stefanski, A., Nakhaei-Rad, S., Kazemein Jasemi, N.S., Al Kabbani, M.A., Gorg, B., Fujii, M., Lang, P.A., Haussinger, D., et al. (2021). Novel FMRP interaction networks linked to cellular stress. FEBS J *288*, 837-860. 10.1111/febs.15443.

69. Collart, M.A. (2016). The Ccr4-Not complex is a key regulator of eukaryotic gene expression. Wiley Interdiscip Rev RNA *7*, 438-454. 10.1002/wrna.1332.

70. Xing, W., Muhlrad, D., Parker, R., and Rosen, M.K. (2020). A quantitative inventory of yeast P body proteins reveals principles of composition and specificity. Elife *9*. 10.7554/eLife.56525.

71. Ito, T., Yang, M., and May, W.S. (1999). RAX, a cellular activator for double-stranded RNA-dependent protein kinase during stress signaling. J Biol Chem *274*, 15427-15432. 10.1074/jbc.274.22.15427.

72. Hoang, H.D., Graber, T.E., and Alain, T. (2018). Battling for Ribosomes: Translational Control at the Forefront of the Antiviral Response. J Mol Biol *430*, 1965-1992. 10.1016/j.jmb.2018.04.040.

73. Li, S., and Sen, G.C. (2003). PACT-mediated enhancement of reporter gene expression at the translational level. J Interferon Cytokine Res *23*, 689-697. 10.1089/107999003772084806.

74. Meyer, C., Garzia, A., Mazzola, M., Gerstberger, S., Molina, H., and Tuschl, T. (2018). The TIA1 RNA-Binding Protein Family Regulates EIF2AK2-Mediated Stress Response and Cell Cycle Progression. Mol Cell *69*, 622-635 e626. 10.1016/j.molcel.2018.01.011.

75. Richardson, S.R., Chan, D., Gerdes, P., Han, J.S., Boeke, J.D., and Faulkner, G.J. (2022). Revisiting the impact of synthetic ORF sequences on engineered LINE-1 retrotransposition. bioRxiv *2022.08.29.505632*. doi: https://doi.org/10.1101/2022.08.29.505632.

76. Goodier, J.L., Mandal, P.K., Zhang, L., and Kazazian, H.H., Jr. (2010). Discrete subcellular partitioning of human retrotransposon RNAs despite a common mechanism of genome insertion. Human molecular genetics *19*, 1712-1725. 10.1093/hmg/ddq048.

77. Hu, S., Li, J., Xu, F., Mei, S., Le Duff, Y., Yin, L., Pang, X., Cen, S., Jin, Q., Liang, C., and Guo, F. (2015). SAMHD1 Inhibits LINE-1 Retrotransposition by Promoting Stress Granule Formation. PLoS Genet *11*, e1005367. 10.1371/journal.pgen.1005367.

78. Huang, Y., Xu, F., Mei, S., Liu, X., Zhao, F., Wei, L., Fan, Z., Hu, Y., Wang, L., Ai, B., et al. (2022). MxB inhibits long interspersed element type 1 retrotransposition. PLoS Genet *18*, e1010034. 10.1371/journal.pgen.1010034.

79. Guo, H., Chitiprolu, M., Gagnon, D., Meng, L., Perez-Iratxeta, C., Lagace, D., and Gibbings, D. (2014). Autophagy supports genomic stability by degrading retrotransposon RNA. Nat Commun *5*, 5276. 10.1038/ncomms6276.

80. Anderson, P., and Kedersha, N. (2009). Stress granules. Curr Biol *19*, R397-398. 10.1016/j.cub.2009.03.013.

81. Standart, N., and Weil, D. (2018). P-Bodies: Cytosolic Droplets for Coordinated mRNA Storage. Trends Genet *34*, 612-626. 10.1016/j.tig.2018.05.005.

82. El Fatimy, R., Davidovic, L., Tremblay, S., Jaglin, X., Dury, A., Robert, C., De Koninck, P., and Khandjian, E.W. (2016). Tracking the Fragile X Mental Retardation Protein in a Highly Ordered Neuronal RiboNucleoParticles Population: A Link between Stalled Polyribosomes and RNA Granules. PLoS Genet *12*, e1006192. 10.1371/journal.pgen.1006192.

83. Kipper, K., Mansour, A., and Pulk, A. (2022). Neuronal RNA granules are ribosome complexes stalled at the pre-translocation state. J Mol Biol *434*, 167801. 10.1016/j.jmb.2022.167801.

84. Krichevsky, A.M., and Kosik, K.S. (2001). Neuronal RNA granules: a link between RNA localization and stimulation-dependent translation. Neuron *32*, 683-696. 10.1016/s0896-6273(01)00508-6.

85. Roy-Engel, A.M. (2012). LINEs, SINEs and other retroelements: do birds of a feather flock together? Frontiers in bioscience (Landmark edition) *17*, 1345-1361.

86. Wallace, N., Wagstaff, B.J., Deininger, P.L., and Roy-Engel, A.M. (2008). LINE-1 ORF1 protein enhances Alu SINE retrotransposition. Gene *419*, 1-6. 10.1016/j.gene.2008.04.007.

87. Jonsson, M.E., Garza, R., Sharma, Y., Petri, R., Sodersten, E., Johansson, J.G., Johansson, P.A., Atacho, D.A., Pircs, K., Madsen, S., et al. (2021). Activation of endogenous retroviruses during brain development causes an inflammatory response. EMBO J *40*, e106423. 10.15252/embj.2020106423.

88. Esnault, C., Maestre, J., and Heidmann, T. (2000). Human LINE retrotransposons generate processed pseudogenes. Nat Genet *24*, 363-367. 10.1038/74184.

89. Newton, J.C., Naik, M.T., Li, G.Y., Murphy, E.L., Fawzi, N.L., Sedivy, J.M., and Jogl, G. (2021). Phase separation of the LINE-1 ORF1 protein is mediated by the N-terminus and coiled-coil domain. Biophys J *120*, 2181-2191. 10.1016/j.bpj.2021.03.028.

90. Sil, S., Boeke, J.D., and Holt, L.J. (2022). Condensation of LINE-1 is required for retrotransposition. bioRxiv, 2022.2004.2011.487880. 10.1101/2022.04.11.487880.

91. Poetz, F., Corbo, J., Levdansky, Y., Spiegelhalter, A., Lindner, D., Magg, V., Lebedeva, S., Schweiggert, J., Schott, J., Valkov, E., and Stoecklin, G. (2021). RNF219 attenuates global mRNA decay through inhibition of CCR4-NOT complex-mediated deadenylation. Nat Commun *12*, 7175. 10.1038/s41467-021-27471-6.

92. Naufer, M.N., Callahan, K.E., Cook, P.R., Perez-Gonzalez, C.E., Williams, M.C., and Furano, A.V. (2016). L1 retrotransposition requires rapid ORF1p oligomerization, a novel coiled coil-dependent property conserved despite extensive remodeling. Nucleic Acids Res *44*, 281-293. 10.1093/nar/gkv1342.

93. Panasenko, O.O., and Collart, M.A. (2011). Not4 E3 ligase contributes to proteasome assembly and functional integrity in part through Ecm29. Mol Cell Biol *31*, 1610-1623. 10.1128/MCB.01210-10.

94. Panasenko, O.O., Somasekharan, S.P., Villanyi, Z., Zagatti, M., Bezrukov, F., Rashpa, R., Cornut, J., Iqbal, J., Longis, M., Carl, S.H., et al. (2019). Co-translational assembly of proteasome subunits in NOT1-containing assemblysomes. Nature structural & molecular biology *26*, 110-120. 10.1038/s41594-018-0179-5.

95. Villanyi, Z., Ribaud, V., Kassem, S., Panasenko, O.O., Pahi, Z., Gupta, I., Steinmetz, L., Boros, I., and Collart, M.A. (2014). The Not5 subunit of the ccr4-not complex connects transcription and translation. PLoS Genet *10*, e1004569. 10.1371/journal.pgen.1004569.

96. Clerzius, G., Shaw, E., Daher, A., Burugu, S., Gelinas, J.F., Ear, T., Sinck, L., Routy, J.P., Mouland, A.J., Patel, R.C., and Gatignol, A. (2013). The PKR activator, PACT, becomes a PKR inhibitor during HIV-1 replication. Retrovirology *10*, 96. 10.1186/1742-4690-10-96.

97. Daher, A., Laraki, G., Singh, M., Melendez-Pena, C.E., Bannwarth, S., Peters, A.H., Meurs, E.F., Braun, R.E., Patel, R.C., and Gatignol, A. (2009). TRBP control of PACT-induced phosphorylation of protein kinase R is reversed by stress. Mol Cell Biol *29*, 254-265. 10.1128/MCB.01030-08.

98. Patel, R.C., and Sen, G.C. (1998). PACT, a protein activator of the interferon-induced protein kinase, PKR. EMBO J *17*, 4379-4390. 10.1093/emboj/17.15.4379.

99. Walsh, D., and Mohr, I. (2011). Viral subversion of the host protein synthesis machinery. Nat Rev Microbiol *9*, 860-875. 10.1038/nrmicro2655.

100. De Cecco, M., Ito, T., Petrashen, A.P., Elias, A.E., Skvir, N.J., Criscione, S.W., Caligiana, A., Brocculi, G., Adney, E.M., Boeke, J.D., et al. (2019). L1 drives IFN in senescent cells and promotes age-associated inflammation. Nature *566*, 73-78. 10.1038/s41586-018-0784-9.

101. Doucet-O'Hare, T.T., Rodic, N., Sharma, R., Darbari, I., Abril, G., Choi, J.A., Young Ahn, J., Cheng, Y., Anders, R.A., Burns, K.H., et al. (2015). LINE-1 expression and retrotransposition in Barrett's esophagus and esophageal carcinoma. Proc Natl Acad Sci U S A *112*, E4894-4900. 10.1073/pnas.1502474112.

102. McKerrow, W., Wang, X., Mendez-Dorantes, C., Mita, P., Cao, S., Grivainis, M., Ding, L., LaCava, J., Burns, K.H., Boeke, J.D., and Fenyo, D. (2022). LINE-1 expression in cancer correlates with p53 mutation, copy number alteration, and S phase checkpoint. Proc Natl Acad Sci U S A *119*. 10.1073/pnas.2115999119.

103. Rodic, N., and Burns, K.H. (2013). Long interspersed element-1 (LINE-1): passenger or driver in human neoplasms? PLoS Genet *9*, e1003402. 10.1371/journal.pgen.1003402.

104. Edgar, R., Domrachev, M., and Lash, A.E. (2002). Gene Expression Omnibus: NCBI gene expression and hybridization array data repository. Nucleic Acids Res *30*, 207-210. 10.1093/nar/30.1.207.

105. Martin, S.L., and Branciforte, D. (1993). Synchronous expression of LINE-1 RNA and protein in mouse embryonal carcinoma cells. Mol Cell Biol *13*, 5383-5392. 10.1128/mcb.13.9.5383-5392.1993.

106. Gibson, D.G., Young, L., Chuang, R.Y., Venter, J.C., Hutchison, C.A., 3rd, and Smith, H.O. (2009). Enzymatic assembly of DNA molecules up to several hundred kilobases. Nat Methods *6*, 343-345. 10.1038/nmeth.1318.

107. Mikels, A., Minami, Y., and Nusse, R. (2009). Ror2 receptor requires tyrosine kinase activity to mediate Wnt5A signaling. J Biol Chem *284*, 30167-30176. 10.1074/jbc.M109.041715.

108. Koblan, L.W., Doman, J.L., Wilson, C., Levy, J.M., Tay, T., Newby, G.A., Maianti, J.P., Raguram, A., and Liu, D.R. (2018). Improving cytidine and adenine base editors by expression optimization and ancestral reconstruction. Nat Biotechnol *36*, 843-846. 10.1038/nbt.4172.

109. Dow, L.E., Fisher, J., O'Rourke, K.P., Muley, A., Kastenhuber, E.R., Livshits, G., Tschaharganeh, D.F., Socci, N.D., and Lowe, S.W. (2015). Inducible in vivo genome editing with CRISPR-Cas9. Nat Biotechnol *33*, 390-394. 10.1038/nbt.3155.

110. Han, J.S., and Boeke, J.D. (2004). A highly active synthetic mammalian retrotransposon. Nature *429*, 314-318. 10.1038/nature02535.

111. Sha, Z., Brill, L.M., Cabrera, R., Kleifeld, O., Scheliga, J.S., Glickman, M.H., Chang, E.C., and Wolf, D.A. (2009). The eIF3 interactome reveals the translasome, a supercomplex linking protein synthesis and degradation machineries. Mol Cell *36*, 141-152. 10.1016/j.molcel.2009.09.026.

112. Dobin, A., Davis, C.A., Schlesinger, F., Drenkow, J., Zaleski, C., Jha, S., Batut, P., Chaisson, M., and Gingeras, T.R. (2013). STAR: ultrafast universal RNA-seq aligner. Bioinformatics *29*, 15-21. 10.1093/bioinformatics/bts635.

113. Bendall, M.L., de Mulder, M., Iniguez, L.P., Lecanda-Sanchez, A., Perez-Losada, M., Ostrowski, M.A., Jones, R.B., Mulder, L.C.F., Reyes-Teran, G., Crandall, K.A., et al. (2019). Telescope: Characterization of the retrotranscriptome by accurate estimation of transposable element expression. PLoS Comput Biol *15*, e1006453. 10.1371/journal.pcbi.1006453.

114. Leng, N., Dawson, J.A., Thomson, J.A., Ruotti, V., Rissman, A.I., Smits, B.M., Haag, J.D., Gould, M.N., Stewart, R.M., and Kendziorski, C. (2013). EBSeq: an empirical Bayes hierarchical model for inference in RNA-seq experiments. Bioinformatics *29*, 1035-1043. 10.1093/bioinformatics/btt087.

115. Love, M.I., Huber, W., and Anders, S. (2014). Moderated estimation of fold change and dispersion for RNA-seq data with DESeq2. Genome Biol *15*, 550. 10.1186/s13059-014-0550-8.

116. McGlincy, N.J., and Ingolia, N.T. (2017). Transcriptome-wide measurement of translation by ribosome profiling. Methods *126*, 112-129. 10.1016/j.ymeth.2017.05.028.

117. Santos, D.A., Shi, L., Tu, B.P., and Weissman, J.S. (2019). Cycloheximide can distort measurements of mRNA levels and translation efficiency. Nucleic Acids Res *47*, 4974-4985. 10.1093/nar/gkz205.

118. Langmead, B., Trapnell, C., Pop, M., and Salzberg, S.L. (2009). Ultrafast and memory-efficient alignment of short DNA sequences to the human genome. Genome Biol *10*, R25. 10.1186/gb-2009-10-3-r25.

119. Liao, Y., Smyth, G.K., and Shi, W. (2014). featureCounts: an efficient general purpose program for assigning sequence reads to genomic features. Bioinformatics *30*, 923-930. 10.1093/bioinformatics/btt656.

120. Pressman, N.J. (1976). Markovian analysis of cervical cell images. J Histochem Cytochem *24*, 138-144. 10.1177/24.1.56387.

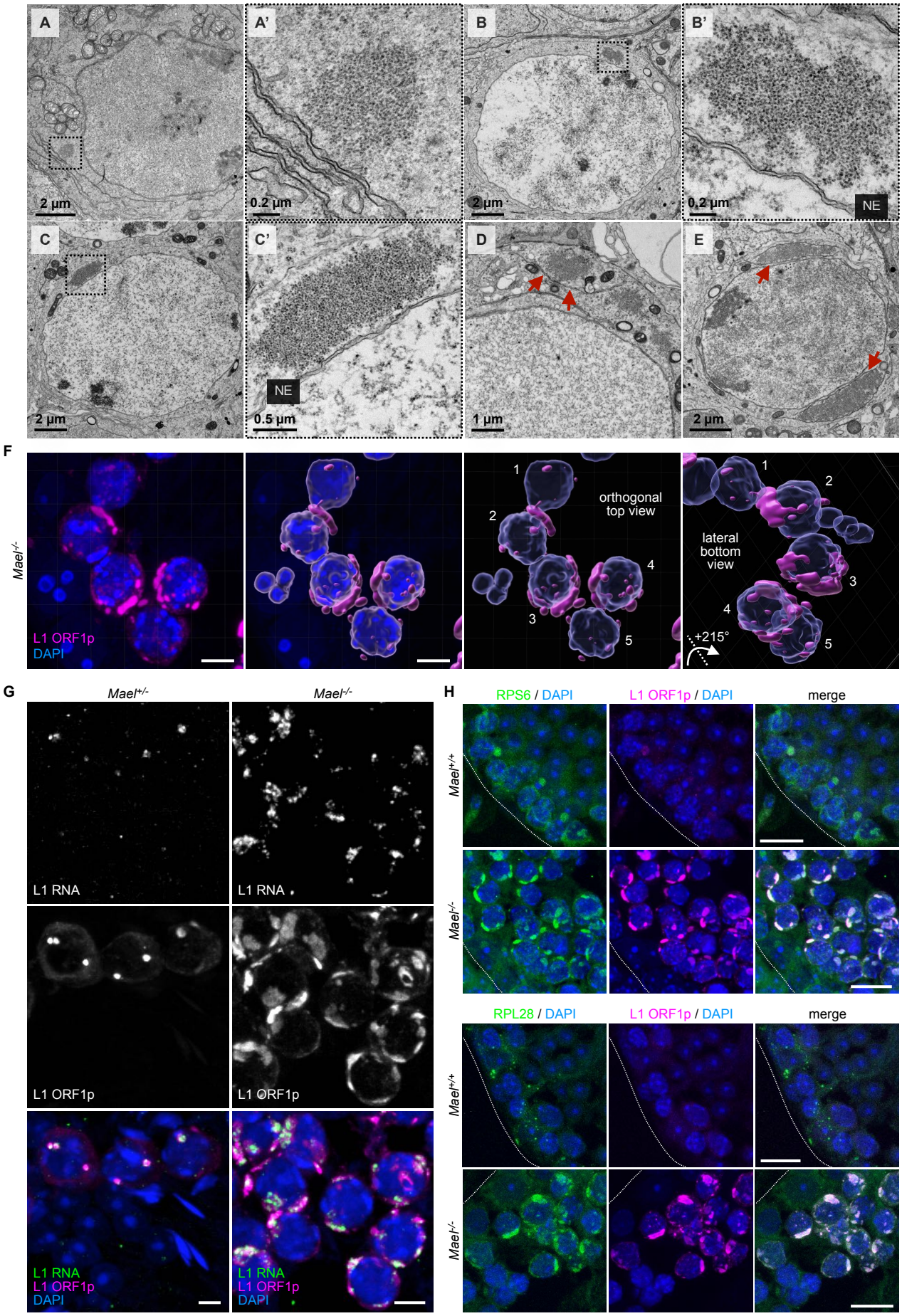
A
A'
B
B'
C
C'
D
E
2 µm
0.2 µm
2 µm
0.2 µm
NE
2 µm
NE
0.5 µm
1 µm
2 µm
F
Mael-/-
L1 ORF1p
DAPI
orthogonal
top view
lateral
bottom
view
+215°
G
Mael+/-
Mael-/-
L1 RNA
L1 RNA
L1 ORF1p
L1 ORF1p
L1 RNA
L1 ORF1p
DAPI
L1 RNA
L1 ORF1p
DAPI
H
RPS6 / DAPI
L1 ORF1p / DAPI
merge
Mael+/+
Mael-/-
RPL28 / DAPI
L1 ORF1p / DAPI
merge
Mael+/+
Mael-/-

Figure 1.

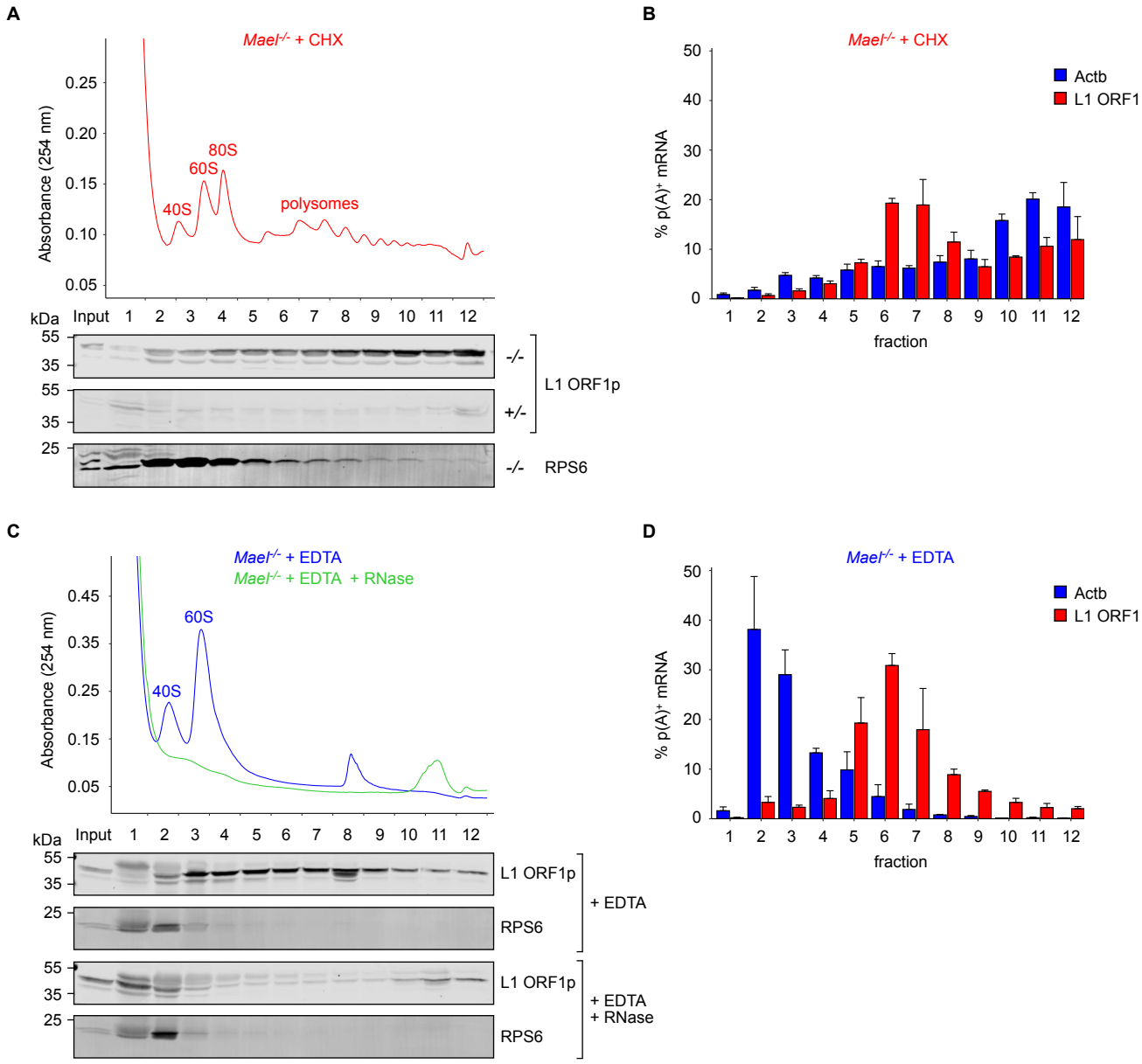
A
Mael-/- + CHX
Absorbance (254 nm)
0.25
0.20
0.15
0.10
0.05
40S
60S
80S
polysomes
kDa
Input 1 2 3 4 5 6 7 8 9 10 11 12
55
35
55
35
25
-/-
+/-
L1 ORF1p
-/- RPS6
B
Mael-/- + CHX
% p(A)+ mRNA
50
40
30
20
10
0
Actb
L1 ORF1
1 2 3 4 5 6 7 8 9 10 11 12
fraction
C
Mael-/- + EDTA
Mael-/- + EDTA + RNase
Absorbance (254 nm)
0.45
0.35
0.25
0.15
0.05
40S
60S
kDa
Input 1 2 3 4 5 6 7 8 9 10 11 12
55
35
25
L1 ORF1p
RPS6
+ EDTA
55
35
25
L1 ORF1p
RPS6
+ EDTA
+ RNase
D
Mael-/- + EDTA
% p(A)+ mRNA
50
40
30
20
10
0
Actb
L1 ORF1
1 2 3 4 5 6 7 8 9 10 11 12
fraction

Figure 2.

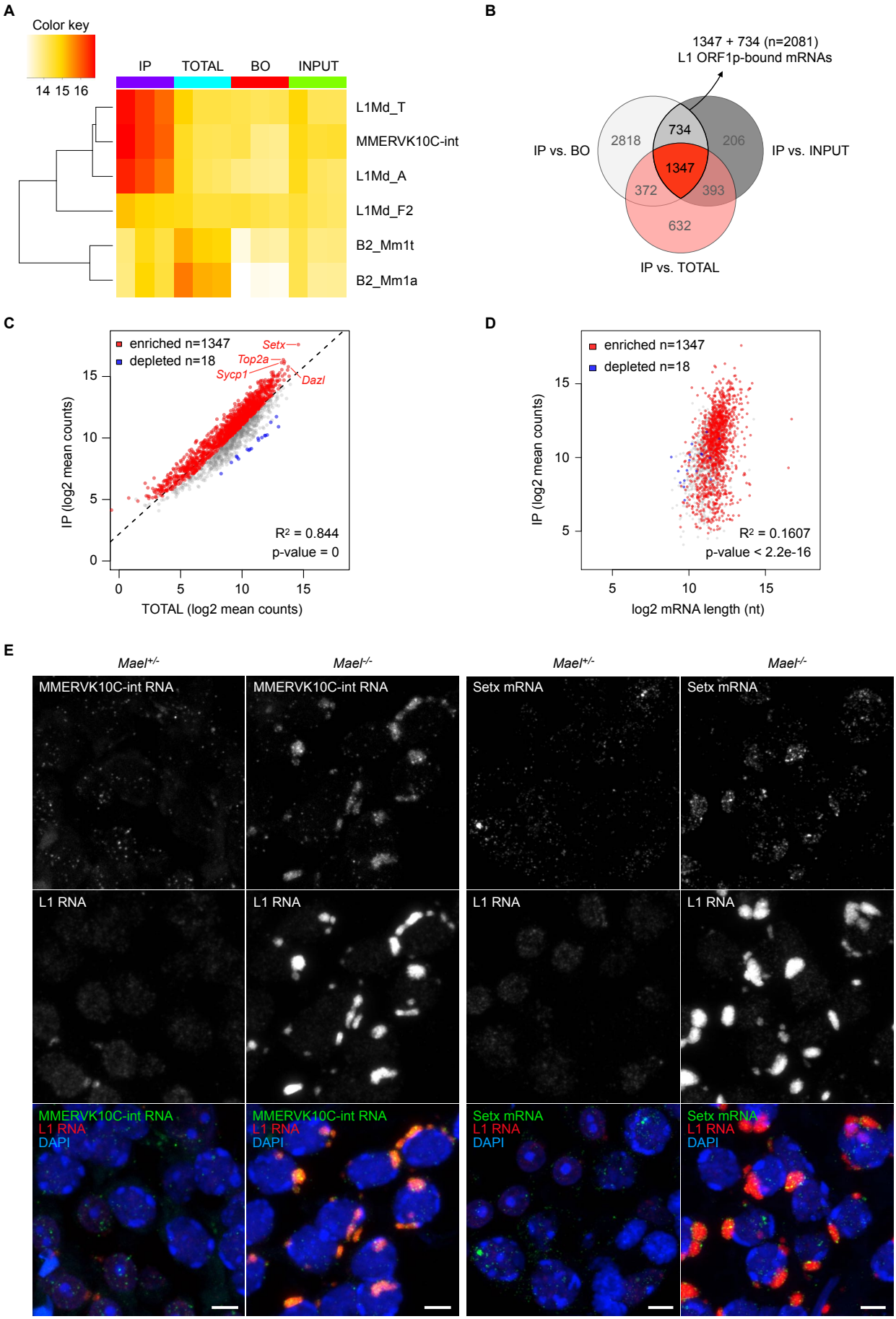
A
Color key
14 15 16
IP
TOTAL
BO
INPUT
L1Md_T
MMERVK10C-int
L1Md_A
L1Md_F2
B2_Mm1t
B2_Mm1a
B
1347 + 734 (n=2081)
L1 ORF1p-bound mRNAs
IP vs. BO
IP vs. INPUT
IP vs. TOTAL
2818
734
206
1347
372
393
632
C
enriched n=1347
depleted n=18
Setx
Top2a
Sycp1
Dazl
R² = 0.844
p-value = 0
IP (log2 mean counts)
TOTAL (log2 mean counts)
D
enriched n=1347
depleted n=18
R² = 0.1607
p-value < 2.2e-16
IP (log2 mean counts)
log2 mRNA length (nt)
E
Mael+/-
Mael-/-
MMERVK10C-int RNA
Setx mRNA
L1 RNA
MMERVK10C-int RNA
L1 RNA
DAPI
Setx mRNA
L1 RNA
DAPI

Figure 3.

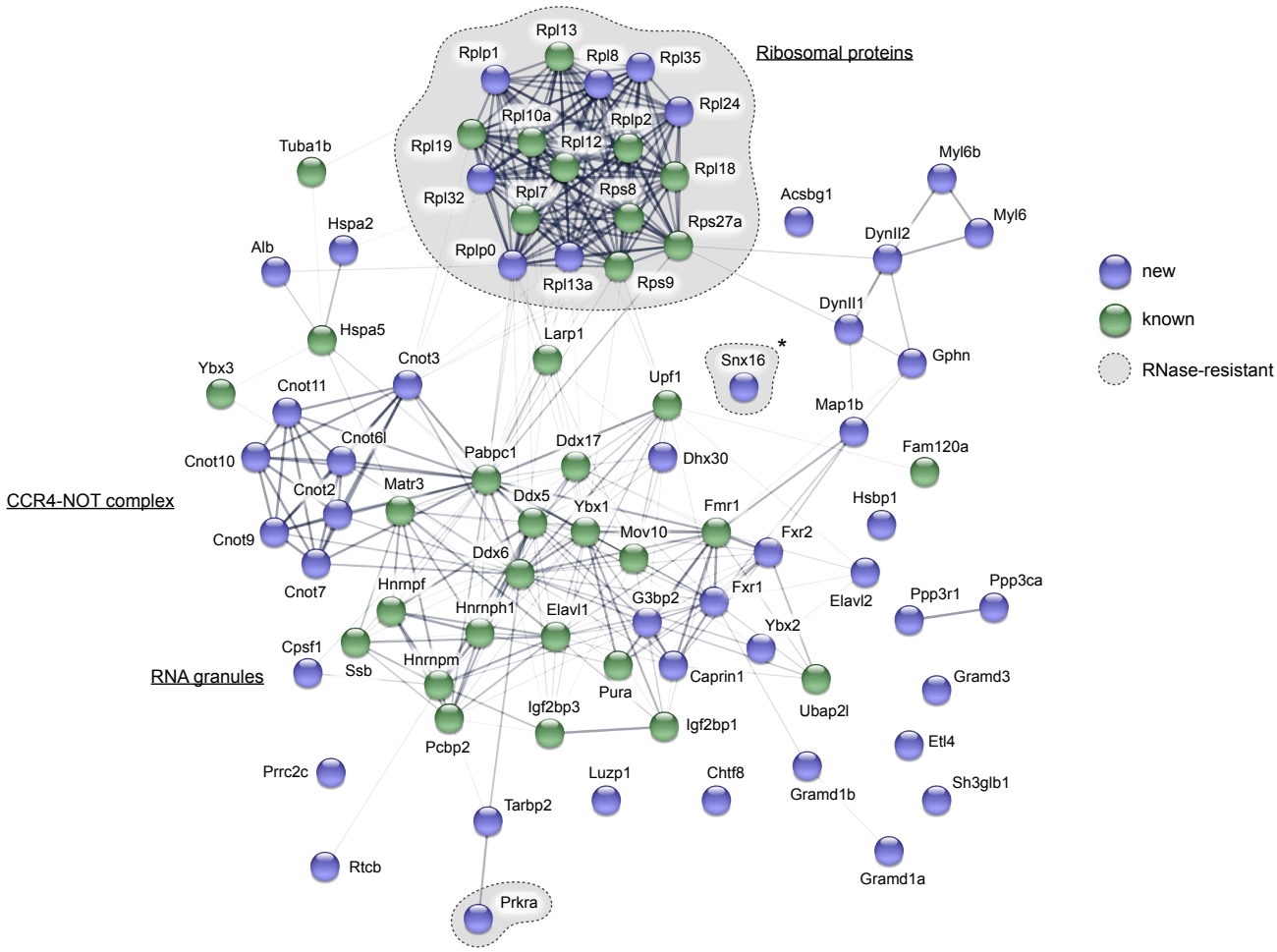
Ribosomal proteins
Rpl13
Rplp1
Rpl8
Rpl35
Rpl24
Rpl10a
Rplp2
Rpl19
Rpl12
Rpl18
Rpl32
Rpl7
Rps8
Rps27a
Rplp0
Rpl13a
Rps9
Tuba1b
Hspa2
Alb
Hspa5
Acsbg1
Myl6b
Myl6
DynII2
DynII1
Gphn
Larp1
Snx16
*
Upf1
Map1b
Fam120a
Ybx3
Cnot3
Cnot11
Cnot6l
Cnot10
Pabpc1
Ddx17
Dhx30
CCR4-NOT complex
Cnot2
Matr3
Ddx5
Ybx1
Fmr1
Hsbp1
Cnot9
Mov10
Fxr2
Ddx6
Cnot7
Hnrnpf
Hnrnph1
Elavl1
G3bp2
Fxr1
Elavl2
Ppp3r1
Ppp3ca
Ybx2
Cpsf1
Ssb
Hnrnpm
RNA granules
Pura
Caprin1
Ubap2l
Gramd3
Igf2bp3
Igf2bp1
Pcbp2
Etl4
Prrc2c
Luzp1
Chtf8
Gramd1b
Sh3glb1
Tarbp2
Rtcb
Gramd1a
Prkra
new
known
RNase-resistant

Figure 4.

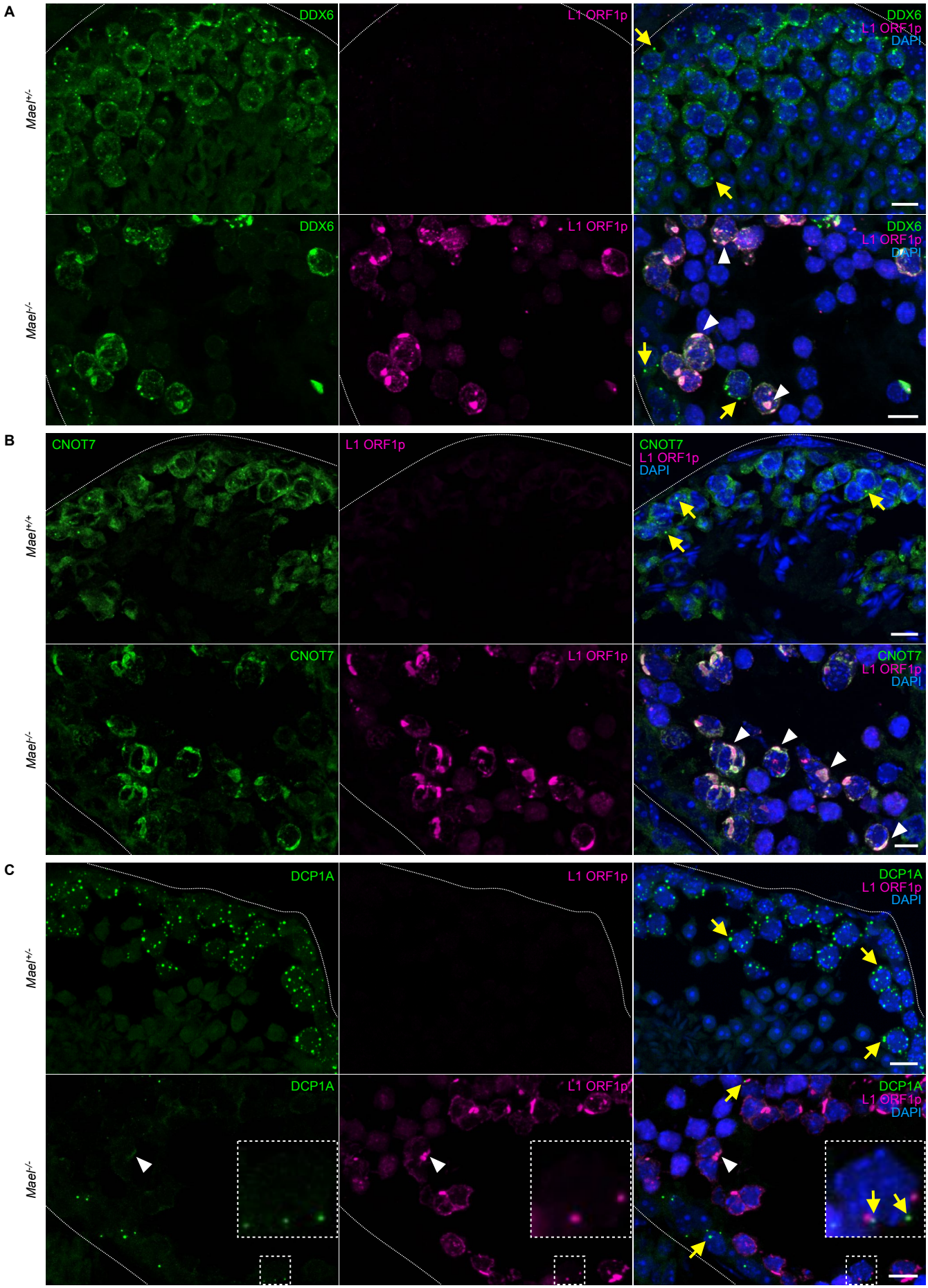
A
Mael+/-
Mael-/-
DDX6
L1 ORF1p
DDX6
L1 ORF1p
DAPI
B
Mael+/+
Mael-/-
CNOT7
L1 ORF1p
CNOT7
L1 ORF1p
DAPI
C
Mael+/-
Mael-/-
DCP1A
L1 ORF1p
DCP1A
L1 ORF1p
DAPI

Figure 5.

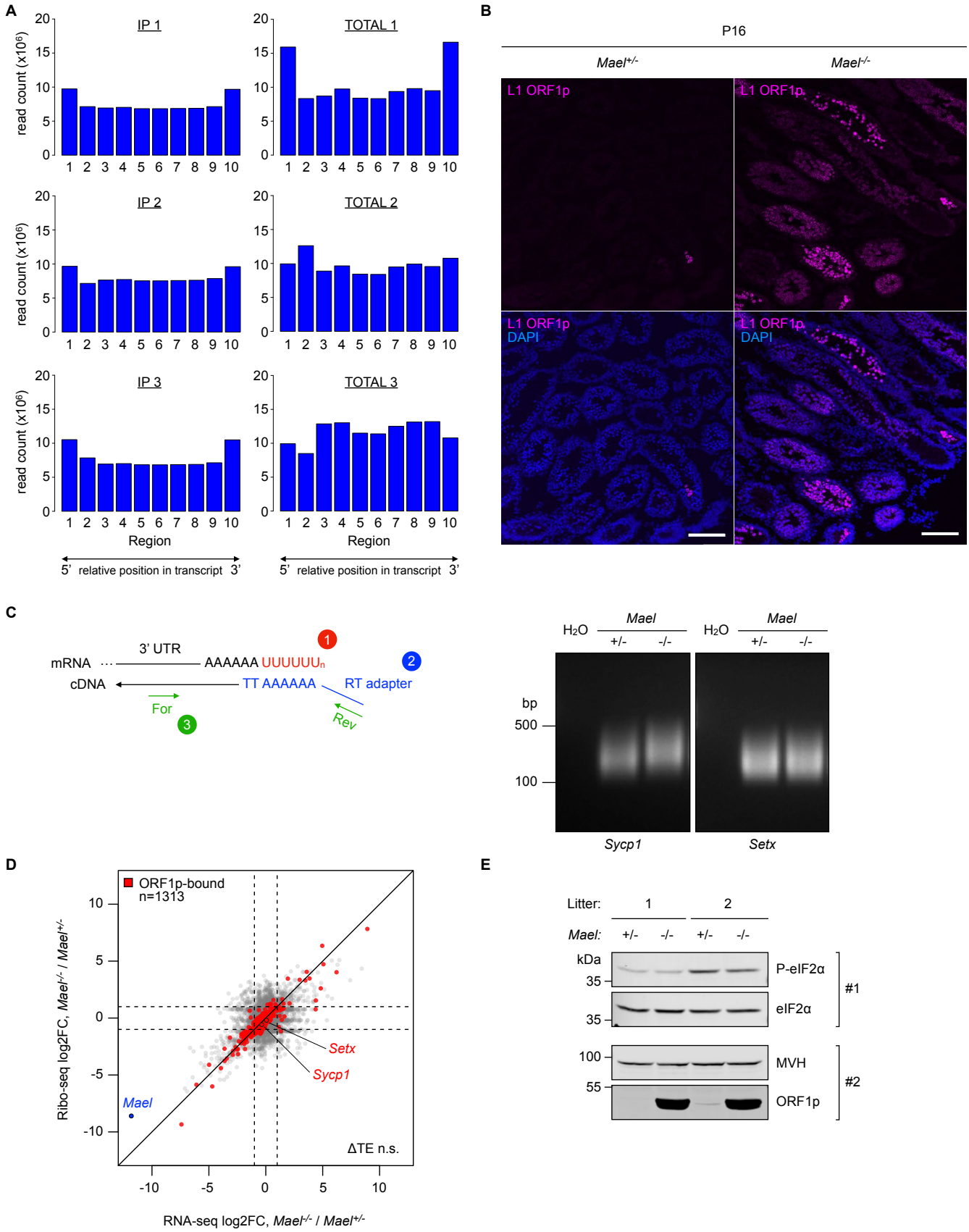
A
IP 1
TOTAL 1
IP 2
TOTAL 2
IP 3
TOTAL 3
read count (x10^6)
Region
5' relative position in transcript 3'
B
P16
Mael+/-
Mael-/-
L1 ORF1p
DAPI
C
3' UTR
mRNA
AAAAAA UUUUUUn
cDNA
TT AAAAAA
RT adapter
For
Rev
H2O
Mael
+/-
-/-
bp
500
100
Sycp1
Setx
D
ORF1p-bound
n=1313
Mael
Setx
Sycp1
ΔTE n.s.
Ribo-seq log2FC, Mael-/- / Mael+/-
RNA-seq log2FC, Mael-/- / Mael+/-
E
Litter:
1
2
Mael:
kDa
P-eIF2α
eIF2α
MVH
ORF1p
#1
#2

Figure 6.

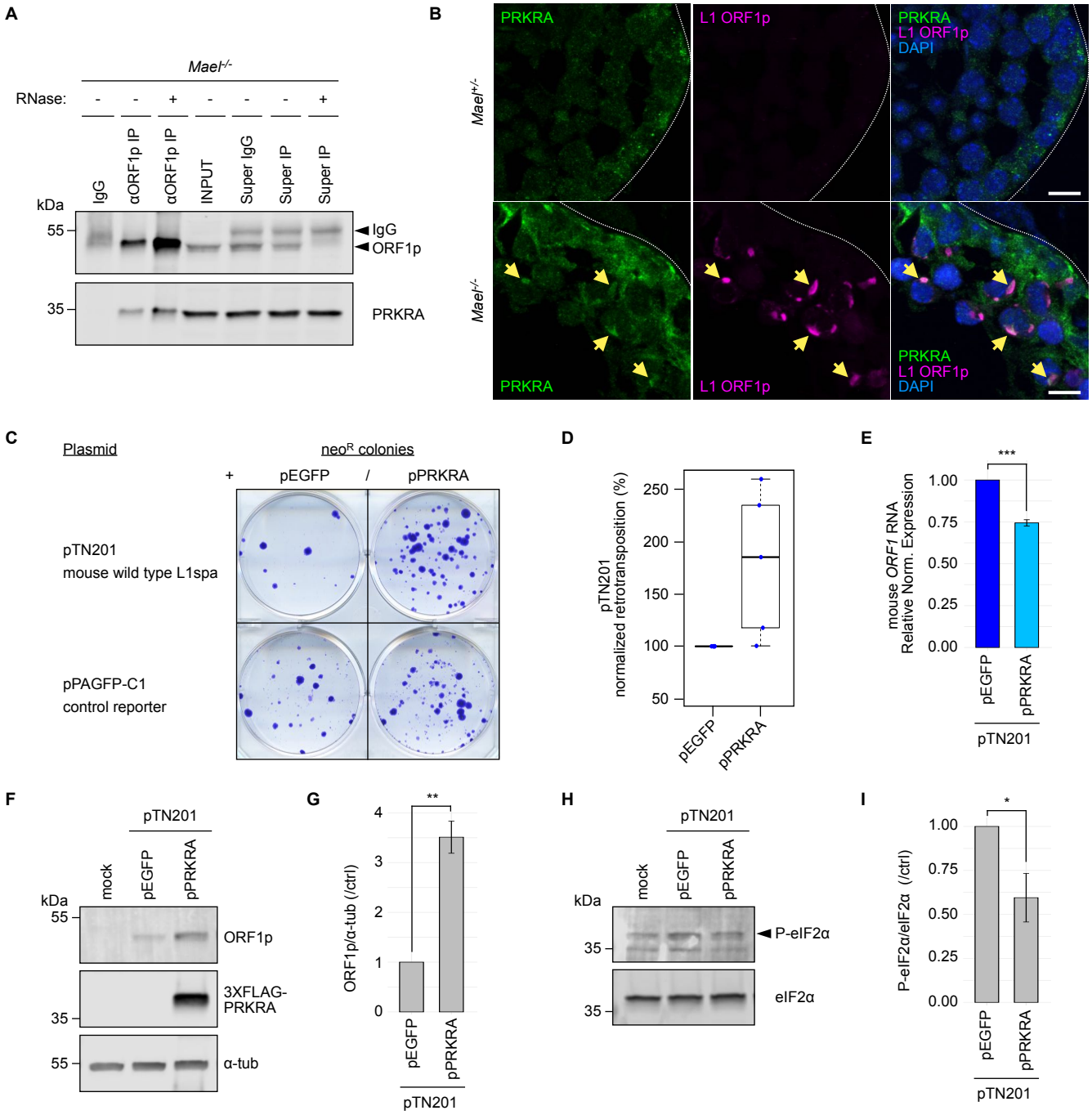
A
Mael-/-
RNase: - - + - - - +
IgG
αORF1p IP
αORF1p IP
INPUT
Super IgG
Super IP
Super IP
kDa
55
35
IgG
ORF1p
PRKRA
B
Mael+/-
Mael-/-
PRKRA
L1 ORF1p
PRKRA
L1 ORF1p
DAPI
C
Plasmid
neoR colonies
+ pEGFP / pPRKRA
pTN201
mouse wild type L1spa
pPAGFP-C1
control reporter
D
pTN201
normalized retrotransposition (%)
250
200
150
100
50
pEGFP
pPRKRA
E
***
mouse ORF1 RNA
Relative Norm. Expression
1.00
0.75
0.50
0.25
0.00
pEGFP
pPRKRA
pTN201
F
pTN201
mock
pEGFP
pPRKRA
kDa
55
35
55
ORF1p
3XFLAG-PRKRA
α-tub
G
**
ORF1p/α-tub (/ctrl)
4
3
2
1
0
pEGFP
pPRKRA
pTN201
H
pTN201
mock
pEGFP
pPRKRA
kDa
35
35
P-eIF2α
eIF2α
I
*
P-eIF2α/eIF2α (/ctrl)
1.00
0.75
0.50
0.25
0.00
pEGFP
pPRKRA
pTN201

Figure 7.